MITIGATING THE EFFECTS OF IONOSPHERIC SCINTILLATION ON GPS CARRIER RECOVERY

by

NATHAN OLIVAREZ

A Thesis
Submitted to the Faculty
of the
WORCESTER POLYTECHNIC INSTITUTE
in partial fulfillment of the requirements for the
Degree of Master of Science
in
Electrical and Computer Engineering
by

MAY 2013

APPROVED:

Professor Alexander Wyglinski, Major Advisor

Professor Andrew Klein

Professor William Michalson

Abstract

Ionospheric scintillation is a phenomenon caused by varying concentrations of charged particles in the upper atmosphere that induces deep fades and rapid phase rotations in satellite signals, including GPS. During periods of scintillation, carrier tracking loops often lose lock on the signal because the rapid phase rotations generate cycle slips in the PLL. One solution to mitigating this problem is by employing decision-directed carrier recovery algorithms that achieve data wipe-off using differential bit detection techniques. Other techniques involve PLLs with variable bandwidth and variable integration times. Since nearly 60% of the GPS signal repeats between frames, this thesis explores PLLs utilizing variable integration times and decision-directed algorithms that exploit the repeating data as a training sequence to aid in phase error estimation. Experiments conducted using a GPS signal generator, software radio, and MATLAB scintillation testbed compare the bit error rate of each of the receiver models. Training-based methods utilizing variable integration times show significant reductions in the likelihood of total loss of lock.

Acknowledgements

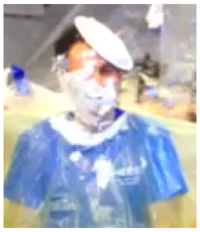

Alexander Wyglinski I would like to thank Prof. Wyglinski for partaking in the role as my advisor, providing wireless communications expertise, research assistance, reviewing my thesis, and letting me pie him on Pi day (in order to relieve some stress).

Andrew Klein Prof. Klein, thank you for introducing me to the fascinating field of digital communications and teaching me everything I know about carrier recovery and communications systems.

William Michalson Many thanks to Prof. Michalson for lending me his GPS signal generator and for insightful conversations and suggestions to help improve my GPS receiver.

Travis Collins Travis, another MS student under Prof. Wyglinski, thank you for the much-needed help with GNU Radio, Matlab, and assistance in writing my thesis.

Maddi McFaul Lastly I would like to thank one of my best friends Maddi for her continuous support and helping me keep my sanity during the past year.

Contents

List of Figures

List of Tables

Chapter 1

Introduction and Motivation

A man and his pregnant wife are preparing to depart to the hospital. The husband in his panicked state of mind, forgets the directions. Fortunately OnStar assistance is just a push of a button away and within minutes has GPS turn-by-turn directions. To help his wife relax, he tunes in a classical station on his satellite radio receiver.

In downtown Kandahar, a convoy encounters a roadside improvised explosive device. The lieutenant leading the convoy uses a satellite phone to call the forward operating base for an explosive ordinance disposal team to come to the site and disarm the bomb. In the meantime, a predator drone in the vicinity and flown from Creech Air Force Base in Nevada identifies an alternative route so the convoy can continue to their destination.

In Texas, a fisherman logs onto the National Oceanic and Atmospheric Association's (NOAA's) website to view up-to-date satellite and radar images of the Gulf of Mexico. The pictures show a storm moving north off the Yucatan Peninsula and he plans his route accordingly. As he departs he uses a GPS receiver to stay on course and reach his port.

The future parents, the lieutenant, and the fisherman have never met each other and probably never will but they all have something in common: they are all relying on satellites for everydays tasks. Since Sputnik was launched in 1957, thousands of satellites have been placed into orbit for purposes ranging from positioning, such as the Global Positioning

System (GPS) satellites; entertainment, such as satellite radio and television; weather forecasting, such as the NOAA's geostationary satellite network; communications, such as amateur radio communication and satellite phones; and satellite imagery, both civilian and military use.

1.1 Overview of GPS and Satellite Communications

"Where's Waldo?" The elusive cartoon character seems to always be lost, but thanks to GPS we can know exactly where Waldo is, as well as our vehicles, firefighters, fishing trolleys, aircraft, a shipping container from Korea, weather balloons, troops on the ground, missiles – virtually anything that needs to be located in real time can be located all thanks to GPS. Sputnik, the first artificial satellite launched by the Soviet Union in 1957, paved the way for satellite-based navigation systems. American physicists William Guier and George Weiffenbach discovered the satellite's position could be determined by analyzing the Doppler shift of the transmitted signal [2]. Less than three years later, the U.S. Navy successfully launched the first of six satellites that would comprise the NAVSAT (also known as TRANSIT) constellation. NAVSAT, or Navy Navigation Satellite System, was the first operational satellite positioning system designed for positioning for the U.S. Navy's fleet of ships and submarines [46]. Because the constellation only comprised of 10 satellites, a position fix could only be obtained a few times a day. Additionally processing to determine a position was computationally intensive, but could determine sub-meter accuracy.

Figure 1.1: GPS Satellite [28]

In use until 1996, NAVSAT service was phased out beginning in 1978 by a new type of navigation system based on timing. TIMATION, the predecessor to modern-day GPS, was first launched in 1967 and was the first satellite to utilize an on-board atomic clock [32]. Unlike NAVSAT which determined the position using each satellite signal's Doppler shifts, TIMATION uses the time difference of arrival between satellites to determine a position fix. The orbits of each satellite were selected to maintain consistent ground track so that each satellite's position would repeat periodically and be predictable. TIMATION was largely a testbed used for developing the standards and technology that would be used for the Global Positioning System (GPS), the system still in use today. GPS utilizes newer electronics and a larger constellation that allows for continuous coverage. Unlike TIMATION, each GPS satellite transmits an almanac containing its current location, which is necessary to accurately compute the pseudorange and establish a position fix [17].

1.1.1 Problems with Satellite Communications

Ever since Samuel Morse sent the first telegraph in 1838, society has yearned to increase the range of communications to reach anyone, anywhere. The laying of the transatlantic telegraph line in 1861 was a huge benchmark in linking communication between the Americas and Europe. In 1876, Alexander Graham Bell demonstrated the first successful operation of the telephone which showed that people can talk to each other, no matter how far apart they are. The invention of the first mobile phone in 1946 and and the advanced mobile phone system (AMPS) in 1983 [25] further extended the limits of interpersonal communications. The invention of the internet took communications to an entirely new level, allowing people to communicate with several people at a time – either a select few via email and instant messaging or millions via a public website or social networking. The development of mobile data services such as 3G, Wi-Max, and 4G LTE [1], [10] enables subscribers to access all of this content wirelessly, anywhere there is coverage. With over 1.2 billion mobile broadband subscriptions worldwide [16], we are fast approaching an era where anyone can communicate with anyone else in the world.

Despite these advances in expanding communication systems, there are many factors that limit their reach. For example, obstructions between base stations cause path loss. Path loss is the attenuation of the power spectral density of an electromagnetic signal. Path loss in direct line of sight communication can be modeled using the Friis transmission equation:

$$P_r = P_t + G_t + G_r + 20 \log_{10} \frac{\lambda}{4\pi R} \tag{1.1}$$

where P_r is the received power, P_t is the transmitted power, G_t is the transmitter antenna gain, G_r is the receiver antenna gain, λ is the signal wavelength, and R is the distance between the two antennas [31]. As shown, the signal attenuation increases logarithmically as the distance increases. When obstacles are present, such as walls, windows, buildings and mountains, a direct line of sight path is not possible which greatly increases the signal attenuation. Increasing the transmit power to improve the signal to noise ratio is one way to help resolve this problem. Another method is to strategically place the transmit and receive antennas so as to minimize the path loss. For example, cellular phone towers are often placed atop tall buildings; increasing the height reduces the number of obstructions and in turn improves the coverage area.

Another common problem is multipath interference. Multipath is when an electromagnetic signal is reflected and the receiver detects multiple copies of the original signal, all coming from different directions. This can cause problems when the copies destructively interfere with one another which causes fading. Reflections can also pose problems for receivers used in localization applications, such as GPS receivers, since they operate by accurately measuring the time of arrival of a signal. Smart algorithms can be implemented at the receiver to mitigate the problems associated with multipath. Using various statistical models, including Rayleigh distributions and Rician distributions, it is possible to determine which signals are reflections and which one is the original [12].

1.1.2 Problems Pertaining to GPS

GPS suffers from many of the same problems encountered by mobile telecommunications systems and other satellite links. In many ways, however, GPS is far more susceptible to the problems of fading and multipath because the low-powered, spread spectrum signals are transmitted beneath the noise floor. GPS satellites operate higher than any ground antenna and thus have a large coverage area. However with a large coverage area comes many opportunities for obstructions to interfere with the signal.

The primary interfering obstacle is the atmosphere itself, or more specifically, the particles in the atmosphere. The ionosphere is filled with charged particles called ions, hence the name. These ions refract electromagnetic signals changing their direction much like a ray of light is “bent” as it enters a pond. But unlike the pond which has a fixed refractive index, the refractive index of the ionosphere is constantly changing. This phenomenon, known as ionospheric scintillation, is a problem that affects many satellite communication systems, particularly GPS because of its low transmit power. Ionospheric scintillation, caused by the charged particles in the ionosphere, results in the rapid phase and amplitude fluctuations of a signal. The magnitude of refraction and the rate at which it changes depends on several factors including space weather, the current total electron count (TEC), the time of day, geomagnetic activity, and solar activity. Under certain conditions, the signal can be completely reflected resulting in abrupt and significant fades. Although GPS satellites orbit high in the sky and often operate in direct line-of-sight with receivers on the ground, the vast distances the signals must travel between transmitter and receiver creates a large window of opportunity for signal degradation.

1.2 The Problem and Motivation

The goal of this thesis is to address the problem of GPS loss of lock occurring during periods of ionospheric scintillation. A temporary loss of a GPS signal can be a detrimental to the receiver because it can lead to total loss of lock. Several seconds or even minutes can go by before the receiver is able to reacquire the signal and regain lock. This delay poses a serious risk to navigation systems onboard vehicles such as aircraft, guidance systems, and missiles that require current and precise coordinates.

Loss of lock can be triggered by the failure of the carrier tracking scheme in the GPS receiver. Carrier tracking utilizes a locked loop algorithm to maintain an accurate estimate of the carrier frequency. However rapid phase and amplitude fluctuations resulting from scintillation make carrier recovery an arduous task. This thesis investigates several carrier recovery algorithms in an effort to mitigate the effects of ionospheric scintillation on GPS tracking.

1.2.1 Problem Statement

Ionospheric scintillation causes rapid phase and amplitude fluctuations in GPS signals. The combination of simultaneous deep fades and phase rotations creates cycle slipping in the phase locked loops that are used to achieve carrier recovery. Cycle slipping causes the tracking scheme to return an inaccurate estimate of the actual carrier frequency and in some cases can lead to frequency unlock. When frequency unlock occurs, it may be necessary for the GPS receiver to reacquire the signal to regain lock, a process that can take several seconds, even minutes. The purpose of this thesis is to determine methods of improving the robustness of the carrier recovery scheme to maintain accurate tracking during periods of scintillation. Maintaining lock mitigates the need for reacquisition and reduces the overall bit error rate.

1.2.2 Motivation

One of the leading causes of ionospheric scintillation is an increase in the concentration of charged particles in the ionosphere, which is quantified by the total electron count (TEC). Heightened solar activity can lead to solar flares, large bursts of charged particles [27]. When a solar flare reaches Earth, the TEC increases and hence the likelihood that scintillation will occur [23]. A two year case study conducted by the NorthWest Research Associates in 2001-2003 (during the last solar maximum) shows a correlation between heightened solar activity and an increase in ionospheric scintillation [24]. To show this graphically, a map depicting the total electron count measured before (Figure 1.2a) and during (Figure 1.2b) a solar storm was compiled by NASA/Goddard Space Flight Center. On 11 April 2001, a solar storm caused a significant increase in the TEC over much of the continental United States.

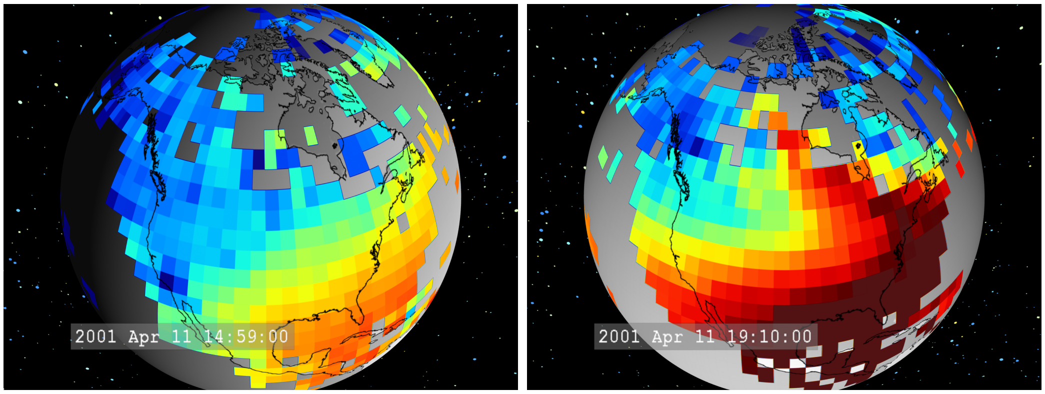

(a) (b)

Figure 1.2: Ionospheric Total Electron Count (TEC) prior to a solar storm (a) and during a solar storm (b). Red indicates high TEC, blue is low TEC, and gray indicates no data available [39].

Periods of heightened charged particle concentration can cause devastating effects to satellite communication systesm, especially GPS [34]. As the 2013 solar maximum is currently underway, there is a need for robust GPS receivers able to operate under the strenuous conditions imposed by the escalated solar activity. This thesis aims to investigate improvements that could be implemented in GPS receivers to help them navigate through the approaching solar storms.

1.3 Research Contributions

- Using existing MATLAB GPS processing scripts and scintillation models, this thesis will develop a testbed for adding a scintillation channel during post-processing. This testbed will be used to replicate scintillation conditions on complex baseband data recorded using the USRP software radio platform.
- This thesis investigates the repeating nature of the GPS frame structure. Decision-directed PLL discriminator algorithms are devised to experiment with using this data

as a training sequence.

- Experimentation with the integration time shows the PLL step size plays an integral role in the receiver's ability to maintain lock on a GPS signal during scintillation conditions. A method is proposed that varies the step size based on the scintillation intensity.
- The results of the experiments show that training-based decision directed PLL algorithms do not outperform the best current receiver models. However, when coupled with variable step sizes, these discriminators show comparable performance to the current state of the art.
- Although this thesis does not determine a method that ultimately improves carrier tracking during periods of scintillation, it does show that it is possible to use prior data as a training sequence that could be utilized to improve receiver robustness under a wide range of operating conditions.

1.4 Thesis Structure

This thesis is organized as follows: Chapter 2 discusses the the GPS signal structure and receiver operation. Next ionospheric scintillation will be explained, including the types of scintillation, its causes, and how it effects GPS signals. Next existing scintillation models will be explored in order to better characterize its effects and develop an understanding of its properties. The most current receiver models and carrier tracking algorithms will investigated to determine the best approach to designing an improved algorithm. Chapter 3 describes the implementation of the GPS receiver and scintillation testbed. This chapter discusses the design considerations and methodology used for creating new tracking methods. Chapter 4 explains the experiments used to characterize the performance of each receiver model and provides the results from each experiment. Chapter 5 provides a conclusion, an overview of the results, and future work.

Chapter 2

GPS, Scintillation, and Receivers

The purpose of this chapter is to provide an overview of GPS, a background on ionospheric scintillation, and describe the current state of the art in receiver design. The first section will describe the GPS signal spectrum, modulation schemes, and navigation data protocol. Next a generic GPS receiver is reverse-engineered in order to describe its individual components. The third section characterizes the properties and effects of ionospheric scintillation, particularly as it pertains to GPS signals. This section will also detail several scintillation models. Finally the current state of the art in GPS receiver methods will be compared and used to form a basis for developing an improved tracking algorithm.

2.1 GPS Signal Properties

The GPS signal can be described in terms of its spectrum as well as the frame structure of the data. This section describes the transmission properties of the GPS signals, discusses the modulation scheme of the navigation data, and illustrates the protocol for transmissions. Details on the protocol layer, including the preamble, parity check, and message structure, will be elaborated.

GPS signals have a 2 MHz bandwidth and are transmitted on the L1 and L2 bands, 1.57542 GHz and 1.2276 GHz, respectively. The L1 band is the public band utilized by consumer GPS receivers often used in cell phones and navigation products. The L2 band is encrypted, has a higher level of precision, and is primarily used by the military. The L2C band, a civilian (unencrypted) channel is in the process of being introduced to the GPS constellation and is scheduled to become fully operational in 2016 [29]. Utilizing two frequencies will help to improve accuracy and mitigate many of the problems created because of the ionosphere. However because the system is not currently fully operational or available to many receiver units, this thesis will focus only on designs utilizing the single L1 frequency band.

GPS utilizes CDMA (Code Division Multiple Access) as the channel access method. Every satellite vehicle (SV) in the GPS constellation has a unique Course/Acquisition (C/A) code, also known as a pseudorandom noise code, or PRN code, which is highly orthogonal to every other satellites' PRN codes. This spreading sequence is modulated on to the L1 and L2C carriers. (Note that only GPS satellites launched since 2005 support transmission on the L2C band; older satellites only utilize L1 for the C/A code.) The Precise code, or P(Y) code, is an encrypted pseudorandom noise code modulated onto the L1 and L2 carriers. This thesis is only concerned with the use of the C/A code and the L1 carrier. A block diagram of the transmitted signal is shown in Figure 2.1.

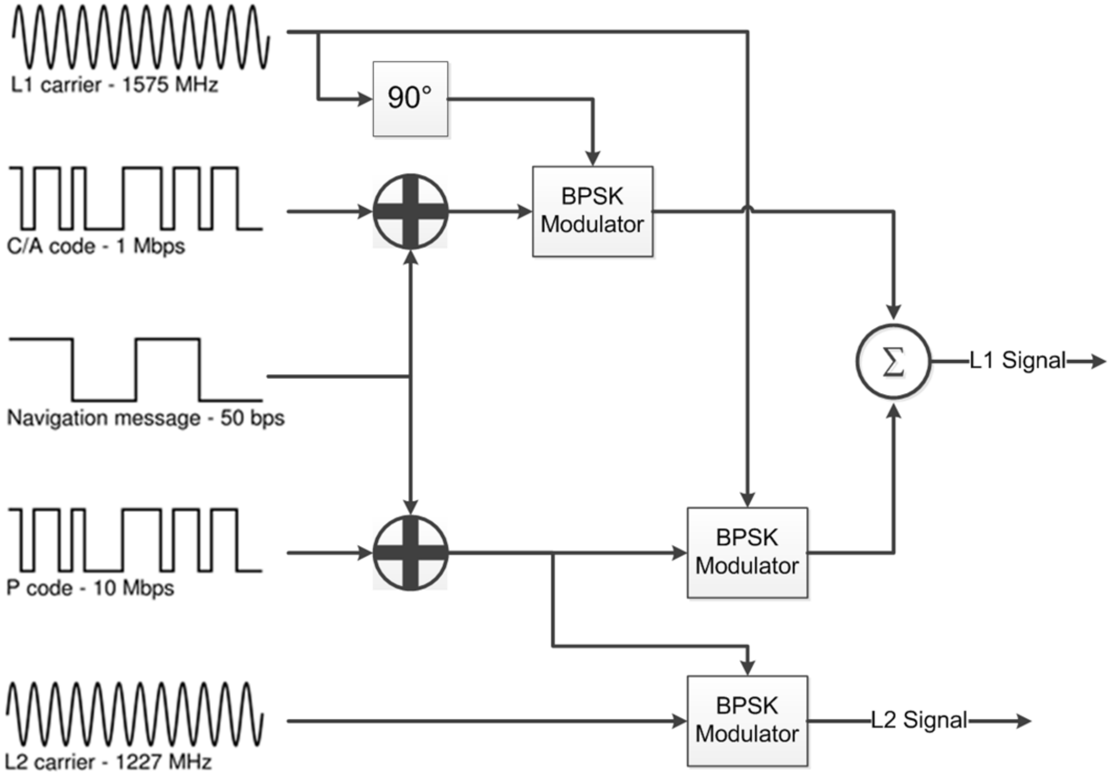

Figure 2.1: GPS signal generation flow diagram. The C/A code is XORed with the navigation message. The sum is modulated using BPSK and the L1 carrier. Simultaneously the P code (encrypted) is XORed onto the navigation message. This message is transmitted both on its own frequency (L2 signal) and added 90 degrees out of phase with the C/A code on the L1 channel.

The C/A code is 1023 bits long and repeats every millisecond at 1.023 MHz. Note that the C/A code does not contain any usable information, it is simply used for acquisition and detection of the signal at the receiver. Acquisition and code tracking will be discussed in detail in the following sections. The navigation data is transmitted at a a much lower frequency of 50 Hz. Each bit lasts 20 ms and the C/A code repeats 20 times. Table 2.1 summarizes these GPS frequencies.

Table 2.1: GPS Frequencies

Component	Description	Frequency	Timing
L1 Band	Public GPS Carrier	1.57542 GHz	n/a
L2 Band	Encrypted GPS Carrier	1.2276 GHz	n/a
C/A Code	Pseudorandom Spreading Sequence	1.023 MHz	Repeats every 1 ms
Data	Navigation Information	50 Hz	20 ms period

The transmitted data is packaged in a frame structure that consists of handover words and the actual navigation data. Each frame of data contains five subframes each 300 bits long. Each subframe lasts 6 seconds because the data is transmitted at 50 Hz. Subframes are further divided into 10 words, each 30 bits long. The first two words of every subframe contain the telemetry (TLM) and handover word (HOW) pair. The telemetry contains an 8-bit preamble (`10001011`) used for frame synchronization, followed by 16 reserve bits and 6-bit parity used to check that the receiver has interpreted the data correctly. Every 30 bit word contains a 6-bit parity at the end. The telemetry structure is shown below in Figure 2.2.

<table>
<tr><td>1</td><td>2</td><td>3</td><td>4</td><td>5</td><td>6</td><td>7</td><td>8</td><td>9</td><td>10</td><td>11</td><td>12</td><td>13</td><td>14</td><td>15</td><td>16</td><td>17</td><td>18</td><td>19</td><td>20</td><td>21</td><td>22</td><td>23</td><td>24</td><td>25</td><td>26</td><td>27</td><td>28</td><td>29</td><td>30</td></tr>
<tr><td colspan="8">Preamble
1 0 0 0 1 0 1 1</td><td colspan="16">Reserved</td><td colspan="6">Parity</td></tr>
</table>

Figure 2.2: Telemetry (TLM) bit structure. The top row shows the corresponding bit number. The first 8 bits contain the preamble, ‘10001011’, the next 16 bits are reserved, and the last 6 bits are used for the parity check.

The handover word contains the 17 most significant bits (MSBs) of the time of week (TOW) and 3 bits indicating the subframe number. The TOW, also known as the Z-count refers to the time that has elapsed since midnight between Saturday and Sunday of the current week, measured in 1.5 second intervals. For example, after 6 seconds have elapsed since midnight, the Z-count would be $6/1.5 = 4$. In one week (7 days), 604,800 seconds elapse; the corresponding Z-count is $604{,}800/1.5 = 403{,}200$. Therfore, the maximum Z-count in one week is 403,199, with rollover occurring at 403,200. Note that when represented in binary 403,200 requires 19 bits. Because the HOW repeats every 6 seconds, only the 17 MSBs of the Z-count are necessary. The two LSBs increment every 1.5 seconds and 3 seconds, respectively, therefore they are superfluous. The subframe ID is 3 bits used to indicate the subframe number (1-5). There are four reserve bits followed by a 6-bit parity. The HOW structure is shown below in Figure 2.3.

1	2	3	4	5	6	7	8	9	10	11	12	13	14	15	16	17	18	19	20	21	22	23	24	25	26	27	28	29	30
TOW (17 MSBs of Z-Count)																			Sub-Frame ID					Parity					

Figure 2.3: Handover word (HOW) bit structure. The top row shows the corresponding bit number. The first 17 bits contain the truncated time of week (TOW) which contains the 17 MSBs of the Z-count, bits 20-22 contain the subframe ID, and the last 6 bits are used for the parity check.

Subframe 1 contains clock correction data used to update the local receiver clock and satellite health information which indicates whether or not the satellite is providing accurate information. Subframes 2 and 3 contain the satellite ephemeris parameters which pertain to the satellite orbit and are necessary for computing the satellite position. Each satellite transmits the ephemeris parameters corresponding to its own vehicle. Subframe 4 contains information regarding the ionospheric correction models as well as almanac data; Subframe 5 continues transmission of the almanac. The almanac provides reduced precision ephemeris information for all 32 GPS satellites in the constellation. The purpose of the almanac is to give the receiver a rough approximation as to where to look for the GPS satellites. It takes 12.5 minutes, or 25 frames, to transmit the entire almanac. The data from subframes 1-3 will be the same in all 25 subframes. For example the ephemeris parameters in subframe 2 will be the same in subframe 2 of all 25 frames. Repeating ephemeris every 30 seconds makes it possible for the GPS receiver to quickly begin tracking a satellite regardless of when it turns on, assuming the almanac data is current. However if a GPS receiver has been off for several days, it may take up to several minutes to collect enough almanac data to acquire the satellite and obtain lock again.

The GPS frame structure is shown below in Table 2.4. The first three subframes repeat every 30 seconds [6]. Assuming accurate timing and frame synchronization at the receiver, it may be possible to exploit this repeating data and use it as a training signal for improving tracking performance [9].

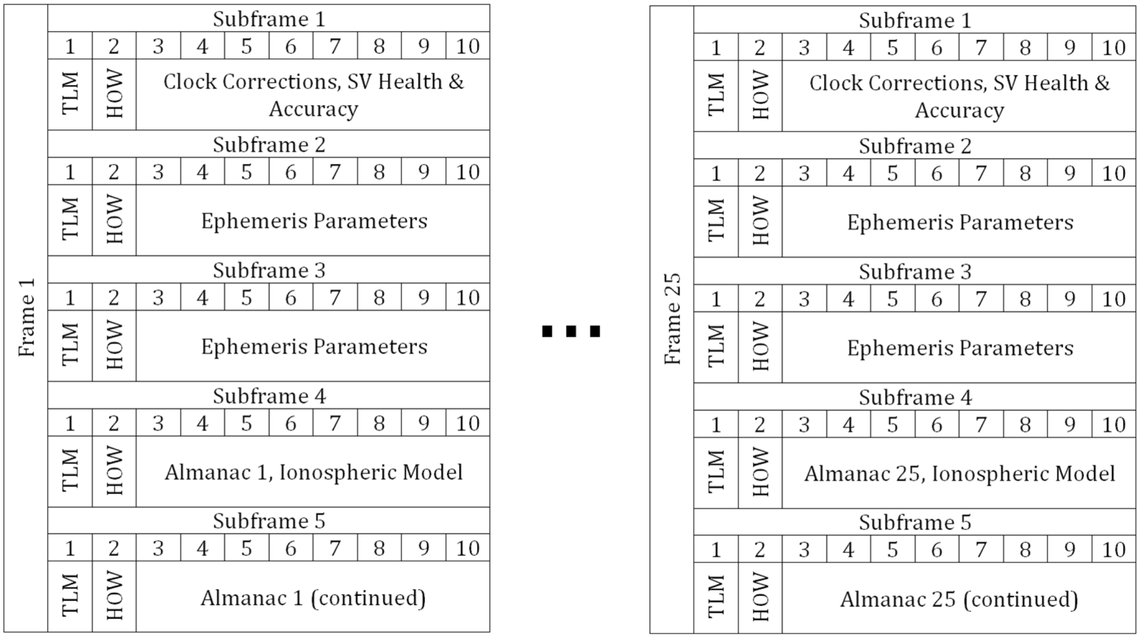

Figure 2.4: GPS frame structure. Frame 1 is shown on the left and Frame 25 is shown on the right; a complete GPS transmission consists of 25 frames, denoted by the '...'. Each frame contains 5 subframes and each subframe contains 10 words. The first two words of each subframe are the TLM and HOW, respectively. The other eight words contain data about the clock, channel, and satellite position.

2.2 GPS Receiver

A typical GPS receiver is a specialized radio designed to utilize the GPS constellation of 32 satellites to provide a position to an end user. An RF front-end is used to receive transmissions on the L1 Band (1575.42 MHz) and demodulate the signal to an intermediate frequency. Processing software acquires signals transmitted from visible satellites and utilizes tracking methods to maintain a lock on each of the signals. Finally, the receiver uses the time of arrival of each signal to compute the position. This section describes how a GPS receiver works by outlining the fundamentals of each of these steps. A simplified

GPS receiver flow diagram is shown in Figure 2.5.

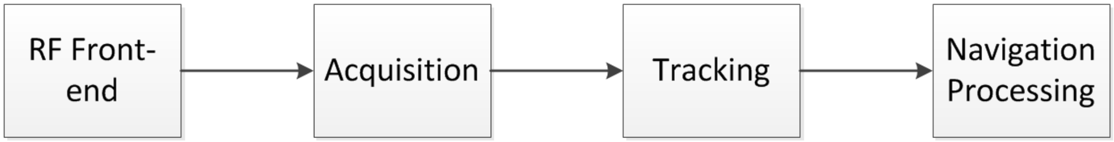

Figure 2.5: GPS high-level receiver flow diagram. The RF front-end receives the transmitted signal and demodulates it to IF. Acquisition determines which satellite vehicles (SVs) are visible and their corresponding carrier and code frequencies. Tracking involves carrier recovery loops that maintain lock on the signal to ensure the data bits are correctly extracted. Navigation uses the data collected from tracking to obtain a position fix.

2.2.1 RF Front-end

The RF front-end is the hardware responsible for collecting and demodulating the L1 GPS signal to an intermediate frequency (IF). Components of the front-end include the antenna, band-pass filter, low noise amplifier (LNA), mixer, and analog to digital converter (ADC). The flow diagram is shown in Figure 2.6.

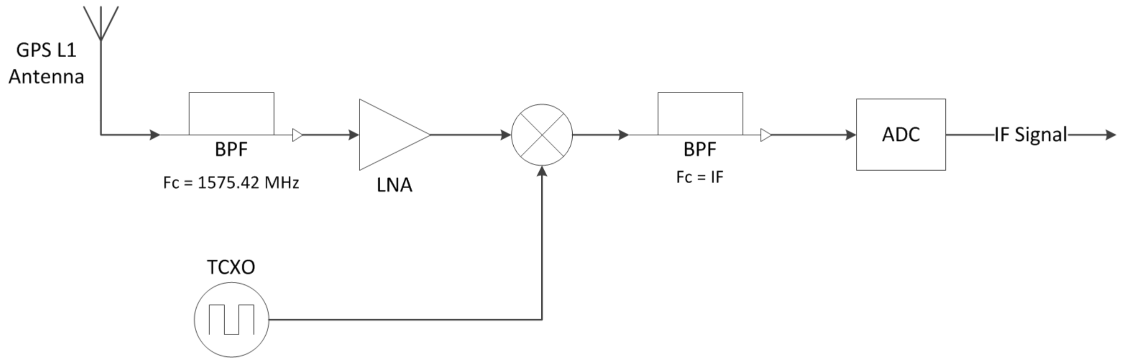

Figure 2.6: GPS RF front-end flow diagram. A GPS antenna (often a patch antenna) is used to collect the signal. A band-pass filter centered at the L1 carrier frequency removes out of band noise. A low noise amplifier boosts the signal power and a mixer demodulates the signal IF using a temperature-controlled oscillator (TCXO). A BPF centered on the IF removes artifacts generated by demodulation. An ADC quantizes the analog signal into digital data that can be used for software processing.

The GPS antenna is an active (powered) patch antenna designed specifically for the L1 band. The antenna provides both passive gain and active gain. Passive gain depends on the surface area of the patch and the size of the ground plane. Since most GPS patch antennas are not omnidirectional and tend to be somewhat directional, the antenna has the highest gain towards higher elevations (and less gain at lower elevations). Active gain depends on the ratio of input to output power. Typical gain ranges from 25 to 50 dB [42]. Figure 2.7 shows a picture of a common GPS patch antenna.

Figure 2.7: GPS Patch Antenna

The GPS L1 signal has a 2.046 MHz bandwidth centered at 1575.42 MHz. However, the receiver bandwidth is generally not this narrow. The purpose of the band-pass filter is to suppress the noise in frequencies outside of the signal bandwidth. If using an ideal filter centered at the carrier's center frequency, only the 2 MHz bandwidth signal would pass through.

The next component, the mixer, is used to demodulate the RF signal to an intermediate frequency or IF. The frequency of the temperature-controlled oscillator (TCXO) affects the resulting IF and must be chosen accordingly. For example, if an IF of 9.55 MHz is desired, the oscillator frequency would be (1575.42 - 9.55)MHz = 1565.87 MHz. However to mix to an IF of 9.55 MHz, a 1565.87 MHz oscillator is not necessary. Instead, a much lower frequency can be used because the signal repeats at integer multiples of the sampling frequency [19]. In this scenario, a sampling frequency of 1565.87/41 = 38.192 MHz can be used instead.

2.2.2 Acquisition

Acquisition is the process of detecting visible satellites and identifying their PRN codes as well as coarse approximations of the carrier frequency and code frequencies. Although all of the GPS satellites are transmitting on the L1 band of 1575.42 MHz, the received frequency will be different for each satellite due to the Doppler shift frequency offset. The Doppler frequency is determined by the line of sight velocity of the satellite with respect to the receiver; satellites moving towards the receiver will have a higher frequency while those moving away will have a lower frequency.

GPS signals from each satellite are separated using a pseudo-random noise (PRN) code. The PRN sequence is also called the coarse acquisition (C/A) code since it is used to acquire coarse approximations of the carrier and code frequencies. As shown in Figure 2.1, each satellite has a uniqe C/A code modulated with the data. All 32 C/A codes are defined in accordance with the GPS Interface Specifications [30] so the receiver knows what C/A codes to expect. Acquisition can be accomplished by correlating the incoming signal with all 32 PRN sequences; sequences with a high correlation indicate the satellite is present.

In practice, the correlation operation is computationally intensive. A suitable alternative is multiplication in the frequency domain, as shown in the flow diagram in Figure 2.8.

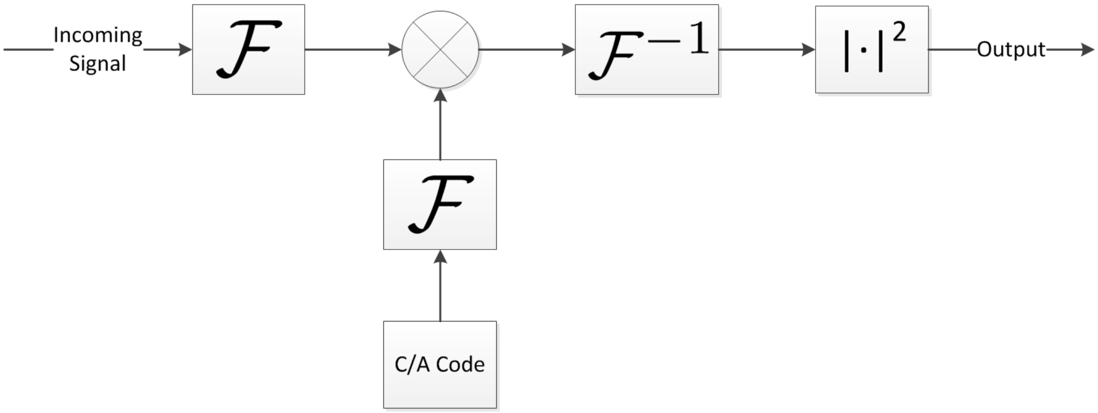

Figure 2.8: Acquisition algorithm block diagram. The incoming signal and C/A code are convolved via multiplication in the frequency domain. The output is the magnitude squared of the inverse Fourier transform.

2.2.3 Tracking

Once the receiver has detected the visible satellites the individual signals must be tracked. Tracking refers to recovering the continuously changing carrier frequency and performing timing recovery with the goal of detecting the transmitted data bits. In its most basic form, the tracking stage can be described in the block diagram shown in Figure 2.9. Tracking consists of two sub-processes: *carrier tracking* and *code tracking*. Carrier tracking is used to generate the carrier wave replica and code tracking is used to generate the C/A code replica.

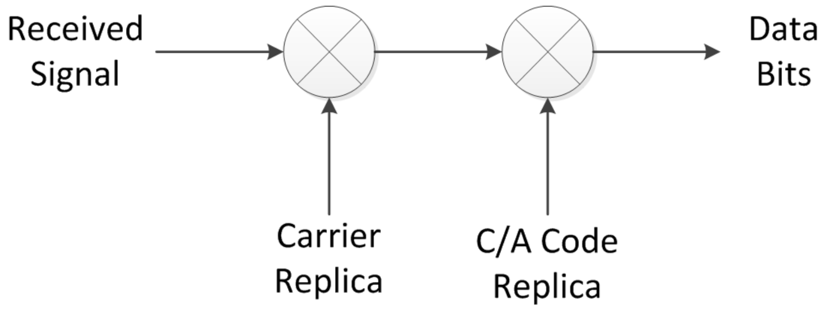

Figure 2.9: Simplified demodulation block diagram. The carrier replica demodulates the IF signal to baseband. The C/A code replica multiplies the baseband signal to extract the data bits.

Carrier Tracking

The purpose of carrier tracking is to determine the carrier frequency and generate a carrier wave replica to demodulate the IF signal to base-band. Although the transmit frequency of 1572.48 MHz is known, there are two main factors which make carrier tracking a necessity in any communications system. First, discrepancies exist between the center frequencies of the transmitter and receiver. Just because a transmitter is tuned to 1572.48 MHz does not mean that is the exact frequency it is receiving; the actual frequency could be off by several kilohertz, an offset large enough that the receiver could miss the GPS signal entirely, if left uncorrected. Therefore one purpose of carrier tracking is to determine this constant frequency offset between the transmitter and receiver. The second factor is frequency changes induced by the channel or other factors such as Doppler shift frequencies. The Doppler shift frequency, and hence the center frequency are never constant because the speed of the satellite relative to the receiver is continuously changing. Channel properties such as multipath, weather, and ionospheric effects are also responsible for affecting the carrier frequency.

The carrier recovery algorithm utilizes a Costas loop to minimize the phase error between the input IF signal and a numerically controlled oscillator (NCO). A block diagram of this model is shown below in Figure 2.10.

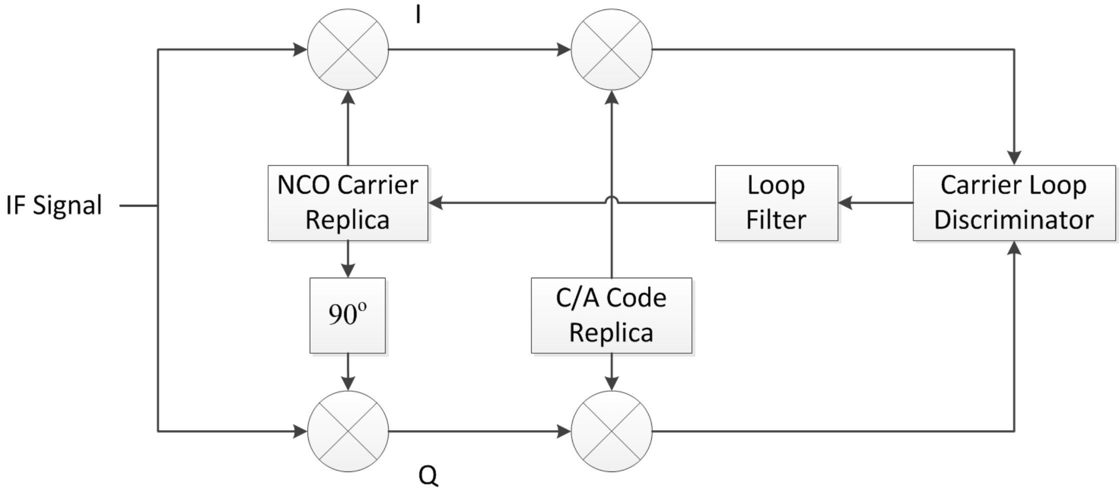

Figure 2.10: Carrier tracking block diagram. The IF signal is demodulated by the carrier replica to extract the in-phase (I) and quadrature (Q) components. These are multiplied by the C/A code to extract the data bits. The I and Q signals are used to generate an error term which updates the frequency of the NCO.

GPS signals rely on the BPSK modulation scheme. Bit transitions are indicated by a 180 degree phase shift in the received signal. Unlike a traditional PLL, the Costas loop can track BPSK signals because it is insensitive to 180 degree phase rotations. As shown in the constellation diagram in Figure 2.11, bits are represented by a +1 or -1 in the in-phase component (bit value of 1 and 0, respectively). Ideally the quadrature component should be zero. The goal of the carrier loop discriminator is to minimize the phase error between the I and Q samples such that none of the signal energy is in the quadrature branch.

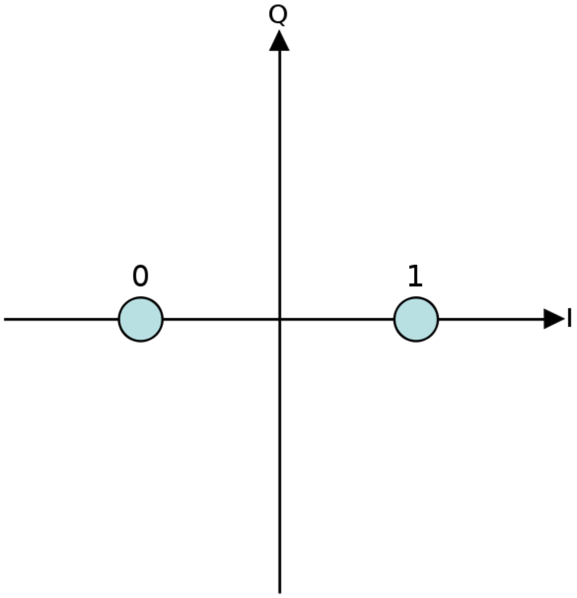

Figure 2.11: BPSK constellation diagram. Bit value ‘1’ is represented by I=1,Q=0 and bit value ‘0’ is represented by I=-1,Q=0.

The carrier loop discriminator algorithms will be discussed in more detail in the following sections.

Code Tracking

The purpose of code tracking is to generate a PRN sequence and keep it aligned with the incoming signal. Since each satellite transmits a unique PRN sequence, code tracking is what allows the receiver to distinguish which satellite the navigation data originated from. Without proper code alignment, data could be misinterpreted which will affect the pseudorange and solution fix computed in the navigation processing. Code tracking is accomplished using a delay locked loop (DLL); a block diagram is shown in Figure 2.12.

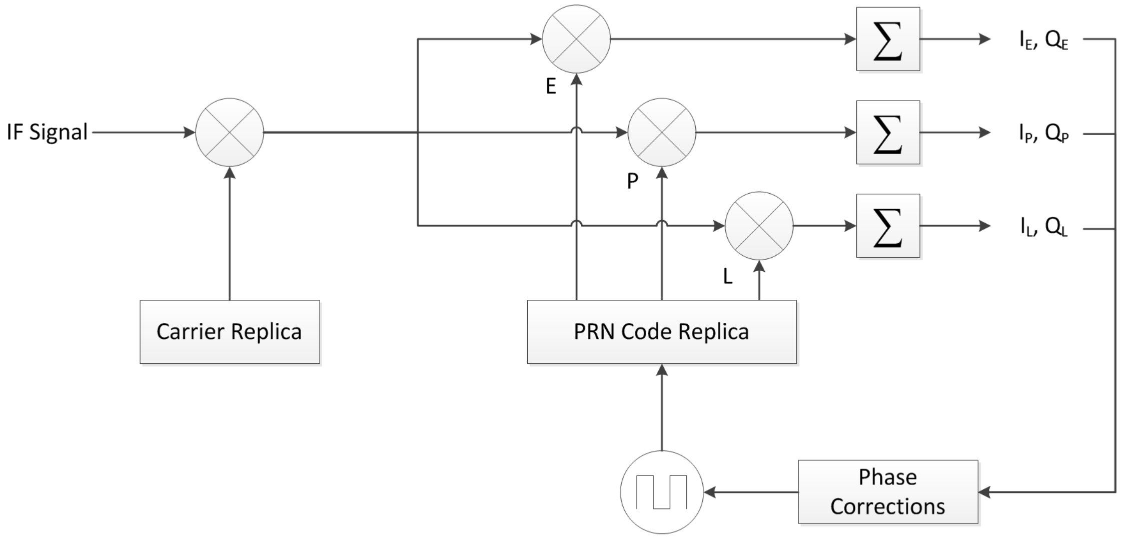

Figure 2.12: Code tracking block diagram. After demodulation, the baseband signal is correlated with shifted versions of the C/A code. The DLL updates the code frequency by maximizing the power in the prompt correlator branch.

A DLL maintains lock by comparing the in-phase and quadrature outputs of the early, prompt, and late correlators ($I_E, Q_E; I_P, Q_P$; and I_L, Q_L, respectively). The DLL uses a discriminator function to generate an error based on the correlator outputs. The goal of the discriminator is to maximize the prompt code output while minimizing the early and late code outputs. There are many types of discriminators that can be used, however the one used in this model is based on the normalized power difference between early and late correlators. The error generated by the discriminator is modeled by:

$$E = \frac{(I_E^2 + Q_E^2) - (I_L^2 + Q_L^2)}{(I_E^2 + Q_E^2) + (I_L^2 + Q_L^2)}. \tag{2.1}$$

This discriminator model is designed to improve code tracking performance in noisy signals [6].

2.2.4 Navigation Processing

Using the preamble of the navigation data it is possible to compute the time of arrival (TOA) of each of the received signals. The receiver then computes the pseudorange to each of the satellites based on the its current ephemeris data. When the navigation data from at least four satellites is accessible, the receiver can find a solution and return a position fix. The navigation processing is beyond the scope of this thesis.

2.3 Ionospheric Scintillation

Unlike cellular phone towers, which are are usually separated by tens of kilometers, satellites are in orbits hundreds of kilometers away from the earth. Signals that travel such distances are susceptible to path loss which reduces the received signal to noise ratio (SNR). In free space, signal attenuation between stations increases logarithmically with respect to their distance. Aside from an occassional bird or plane cruising at 10,000 m, there are few solid obstructions that hinder the transmission of signals to and from satellites orbiting hundreds or thousands of kilometers above the surface of the earth. There are no buildings taller than 1000 m, no mountains taller than 9000 m. So why can't the channel separating satellites and their ground station counterparts be modeled as free space? There are still obstructions, they are just much smaller than a sky scraper or mountain.

The ionososphere is a layer of the atmosphere containing charged particles ionized by solar radiation. Short wavelength light from the sun, including ultra-violet waves and x-rays ionize neutral gas atoms and molecules in this layer. Ionization is when a high energy, high frequency photon separates an electron from its atom or molecule; the result is an electron (negative charge) and a high energy ion (positive charge). This ionization process in the ionosphere creates a plasma layer. A plasma consists of negatively charged electrons and positively charged ions that have too much energy for their electromagnetic force to hold them together. As the density of the charged particles increases, so does the

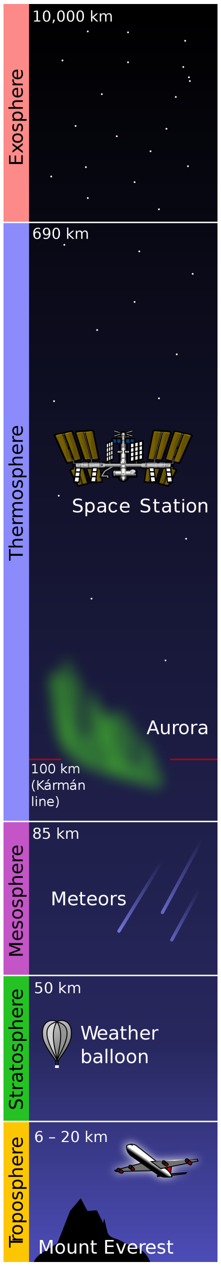

Figure 2.13: Atmosphere layers. The ionosphere consists of the mesosphere, thermosphere, and exosphere [7]

.

likelihood of recombination, the process of an electron spontaneously joining an ion and releasing the energy as a photon, thus rendering the molecule neutral. The ionosphere, depicted in Figure 2.13, is comprised of portions of the mesosphere, thermosphere, and exosphere. Extending from about 50 km to about 2000 km above the earth's surface, it is a large region of charged particles that affects the signals transmitted between satellites and ground stations [40].

This section describes what ionospheric scintillation is, what causes this atmospheric anomaly, how it affects GPS signal reception, and finally methods of characterizing and modeling scintillation.

2.3.1 Scintillation Background

The ionosphere is a layer of plasma located about 50-2000 km above the surface of the Earth. Electromagnetic signals passing through the ionosphere set the charged particles in the plasma in oscillation which causes the radio waves to scatter in different directions, also known as refraction. The refractive index is proportional to the number of charged particles and inversely proportional to the frequency of the signal [40]. Refraction increases in the presence of a higher electron content, and lower frequency signals are refracted more than higher frequency signals. Since the electron concentration is not consistent throughout the path of the radio signal, the refractive index changes at different locations. This refractive index variation causes a phenomenon known as scintillation, the rapid fluctuations in signal strength (amplitude) and phase. A common example of an effect caused by scintillation is the apparent twinkling of stars at night. This phenomenon is depicted in Figure 2.14.

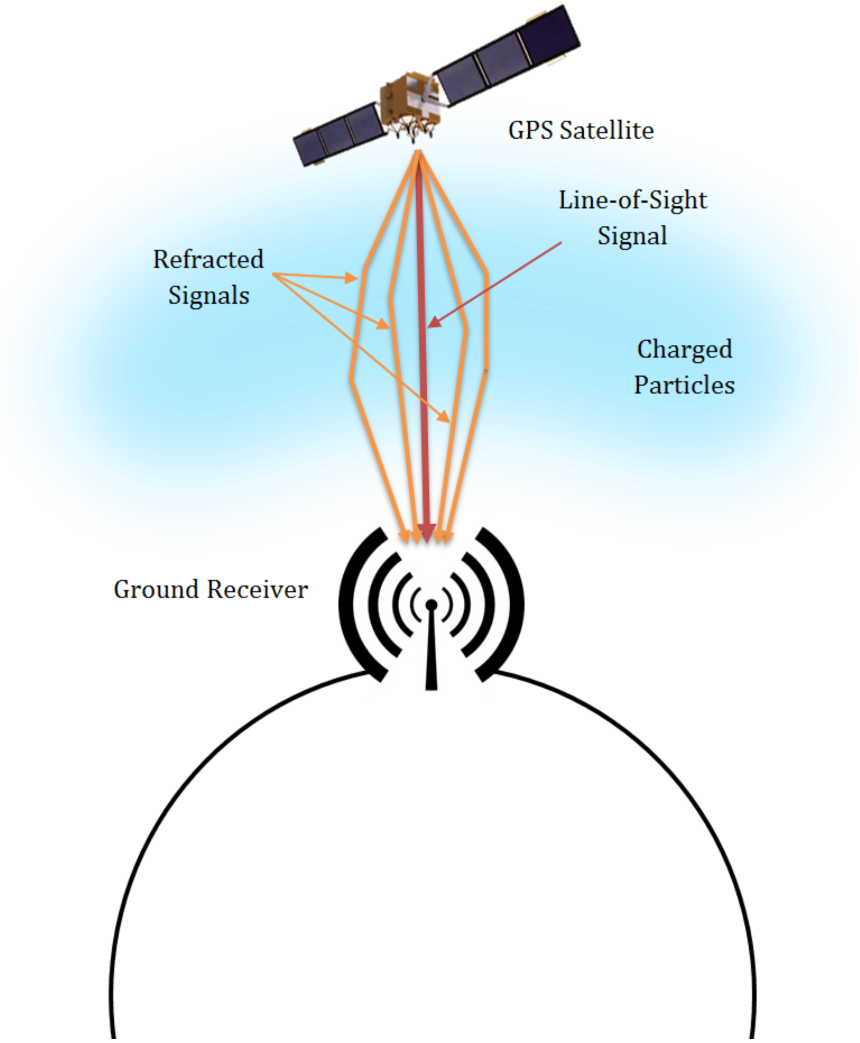

Figure 2.14: Graphical depiction of a GPS satellite and ground receiver. The line of sight signal is shown in red. Refracted signals, resulting from charged particles in the ionosphere, are depicted in orange.

Causes of Scintillation

The electron concentration is affected primarily by the solar wind, solar flares, and electromagnetic radiation from the sun [40]. Solar flares and the solar wind carry charged particles from the sun. When they reach the Earth, some of them are trapped in the Earth's magnetic field, thus adding to the total electron count.The intensity of solar flares and the solar wind is closely related to the number of sunspots which fluctuates on the eleven year solar cycle. Thus, the effects of ionospheric scintillation are increased during the solar maximum and decreased during the solar minimum [5].

Radiation from the sun ionizes particles in the atmosphere thus creating the plasma known as the ionosphere. As the radiation intensity increases, it penetrates further into the atmosphere and hence increases the concentration of electrons and charged particles. Therefore regions of the atmosphere closer to the sun typically have increased electron concentrations; as a result there is a daily mid-day scintillation peak in regions nearest to the equator particularly within the tropics of Cancer and Capricorn. Similarly the total electron count also increases biannually during the spring and autumnal equinoxes when the Earth is most exposed to the sun [5]. It has also been observed that effects of scintillation are very prominent during the evening hours, sometimes even stronger than during the mid-day peak. This is explained by the Appleton anomaly, in which the F layer (also known as the Appleton layer) of the ionosphere has an increase in the number of electrons during the evening hours [8].

Types of Scintillation

Ionospheric scintillation is measured in terms of amplitude scintillation and phase scintillation. Amplitude scintillation is characterized by the S_4 index which is defined as the standard deviation of the signal intensity divided by the average of the signal intensity for a given period of time:

$$S_4 = \frac{\sqrt{\langle I^2 \rangle - \langle I \rangle^2}}{\langle I \rangle} \tag{2.2}$$

where I represents the signal intensity (amplitude squared) and $\langle\rangle$ represents the expected value; for empirical data this is computed as a time average. The S_4 index is a dimensionless number used to represent the scintillation strength. S4 values less than 0.3 indicate weak scintillation and as S4 approaches 0 scintillation becomes nonexistent and does not affect the signal. Although there is no upper limit for the S4 coefficient, values between 0.3 and 0.6 indicate moderate scintillation, and values greater than 0.6 are indicative of strong scintillation and are likely to affect GPS signals.

Phase scintillation, given by σ_ϕ is defined as the standard deviation of a signal's phase over a given time interval. Phase scintillation is computed empirically; values greater than 5° indicate strong phase scintillation [14].

2.3.2 Scintillation Effects on GPS

Ionospheric scintillation is a problem for satellite communications because it affects the amplitude and phase of radio signals. Reducing the amplitude of a radio signal reduces its power level which directly affects the signal to noise ratio, thus hindering a base station's ability to detect and receive the signal. Phase shifts can cause destructive interference in which the crests and troughs of a signal cancel each other resulting is spectral nulls and fading. Fading, the temporary loss of a signal due to attenuation or destructive interference, increases the bit error rate due to lost packets. Scintillation primarily affects GPS signals in the lower latitudes near the equator between +/- 20 degrees latitude [18] as well as in higher latitudes near the poles [43], [38].

GPS signals are particularly vulnerable to ionospheric scintillation primarily because they are low-power spread spectrum signals transmitted below the noise floor. GPS signal strength is typically measured by its carrier to noise density ratio, C/N_0. The signal to noise ratio (SNR) is generally expressed in dB and is a ratio of the signal to noise power in a given bandwidth. C/N_0 on the other hand is expressed in dB-Hz and is a ratio of the signal to noise power per unit bandwidth [20]. The relation between SNR and C/N_0 can be represented by:

$$SNR = \frac{C}{N_0} - BW, \tag{2.3a}$$

or in dB:

$$SNR(\mathrm{dB}) = \frac{C\mathrm{dBm}}{10 \cdot log_{10}(BW) \cdot N_0}. \tag{2.3b}$$

During normal atmospheric conditions, a nominal C/N_0 value acquired by a commercial GPS receiver is about 44 dB-Hz and changes in C/N_0 occur very slowly [13]. The following example relates SNR to C/N_0 during the nominal case. Carrier power C = -130 dBm, the ambient thermal noise density N_0 = -174 dBm/Hz [26], and the receiver bandwidth BW = 4 MHz:

$$SNR = \frac{-130\mathrm{dBm}}{10 \cdot log_{10}(4 \cdot 10^6\mathrm{Hz}) \cdot (-174\frac{\mathrm{dBm}}{\mathrm{Hz}})} = \frac{-130\mathrm{dBm}}{-108\mathrm{dBm}} = -22\mathrm{dB}. \tag{2.3c}$$

However, during periods of scintillation rapid fluctuations of 25 dB or more can occur. Recording stations throughout the lower latitude regions recorded GPS data during the 2001 solar maximum of Solar cycle 23. In one case, GPS data was recorded in Rio de Janiero, Brazil in February 2002. Experiments conducted in [8] show a correlation between periods of GPS signal outages, periods of increased total electron count (TEC), and periods when scintillation was occurring.

Another commonly cited data set was recorded at Ascension Island in March 2001. This data set has been used to generate scintillation models that accurately replicate the frequency of deep fades, the fade duration [37], and the corresponding phase rotations that often occur in conjunction with deep fades [15]. The models developed as a result of these data will be explored in the following sections. Figure 2.15 provides a comparison between nominal conditions and periods of scintillation using data recorded from Ascension Island [37]. The top plot shows nominal C/N_0 and the bottom plot shows deep fades resulting from strong ionospheric scintillation.

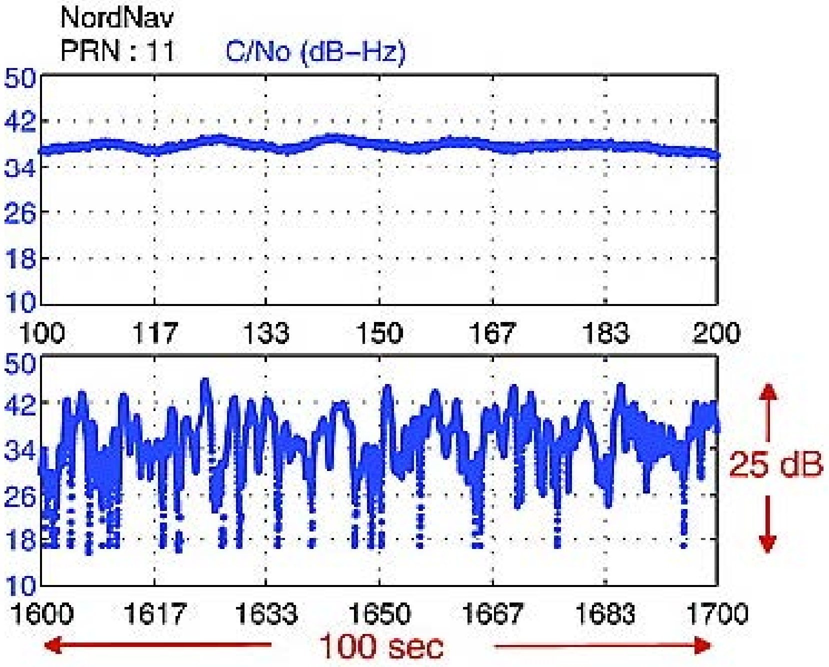

Figure 2.15: Nominal C/N_0 (top), deep fades present at Ascension Island, 18 March 2001 (bottom), retrieved from [37, pp. 2]

Actual GPS data recorded during periods of scintillation is fundamental to developing existing models for ionospheric scintillation and characterizing its properties. One of the properties of scintillation that is most typically responsible for complete loss of lock of the phase tracking loops is a canonical fade. Canonical fades refer to a "power fade of sufficient depth and rapidity that the associated phase time history exhibits an abrupt, near half-cycle phase change" [15]. In other words, canonical fades occur whenever deep fades (amplitude scintillation) and rapid, near-half-cycle phase changes (phase scintillaion) occur simultaneously. Examples of canonical fades are shown in Figure 2.16. These fades are particularly detrimental to carrier tracking loops because the receiver is not able to determine the difference between a phase rotation caused by the BPSK modulation scheme and a phase rotation caused by scintillation.

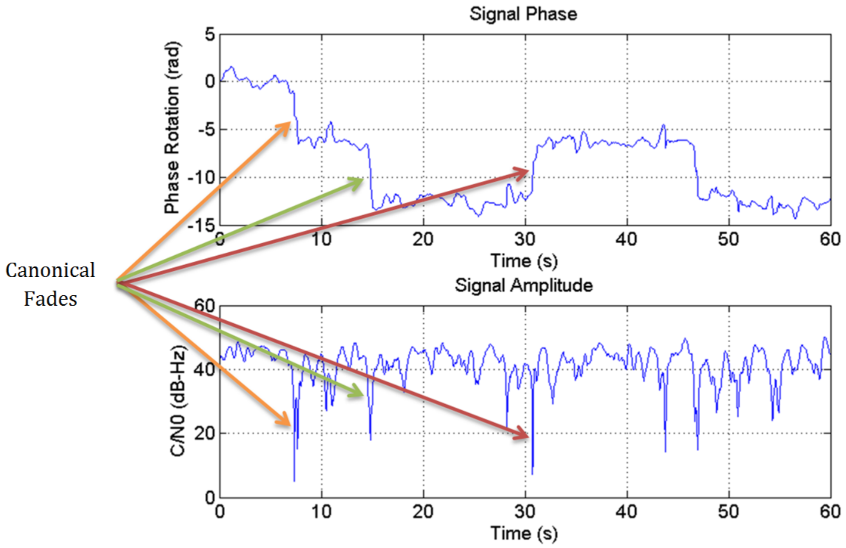

Figure 2.16: Simulated scintillation channel. Top and bottom plots show phase rotation and C/N0, respectively, resulting from scintillation. Arrows denote examples of canonical fades.

Nonsquaring PLLs such as the Costas Loop cannot distinguish the difference between a phase error ϕ and $\phi \pm 2\pi$. An event referred to as a cycle slip occurs when scintillation creates a phase rotation of $\pm 2\pi$. Additionally low SNR makes it increasingly difficult for PLLs to track a signal [3]. When the receiver incorrectly interprets a scintillation-induced phase rotation for a changing bit, the decoded bits will become reversed. The bits will remain reversed until another cycle slip occurs.

A simulated example is shown in Figure 2.17 to demonstrate the effects of a cycle slip. A π radian phase rotation occurs at t=26 ms and t=72 ms. The data bits in between these two times are reversed and may be incorrectly interpreted at the receiver. Figure 2.18 shows a cycle slip example using actual GPS data. Cycle slips occur at about 2.2 s and from 5 - 5.4 s. In both cases, there is some ambiguity as to what the actual decoded bit value should be (blue) compared to the cleanly (no scintillation added) received signal (red). As shown in the bottom plot, the phase error of the PLL slips in increments of 2π. Although in this case the receiver is able to maintain lock on the signal, Figure 2.19 demonstrates a situation in which bit rotations occur as a result of cycle slipping (first occurrence can be seen at t = 2 s) as well as temporary loss of lock (from t = 8-10 s). In an extreme case, Figure 2.20 shows how repeated cycle slips can cause complete loss of lock of the signal. In this case, reacquisition may be necessary in order to continue tracking and demodulation of the navigation data.

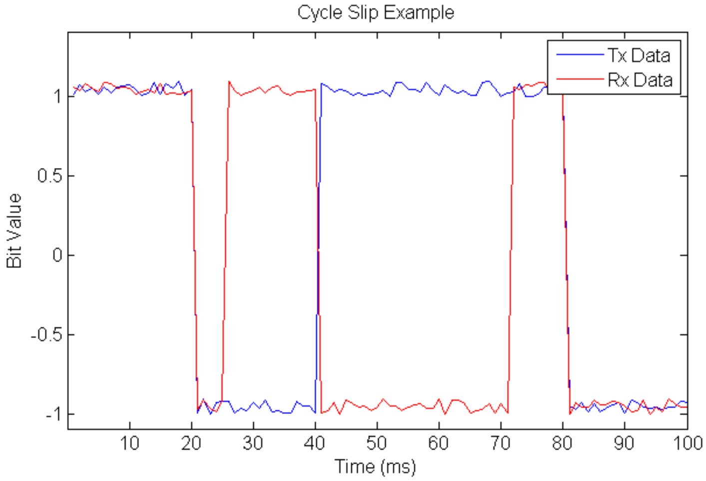

Figure 2.17: Cycle slip example: the transmitted data is shown in blue, the received in red; *pi* phase rotations occur at t=26 ms and t=72 ms.

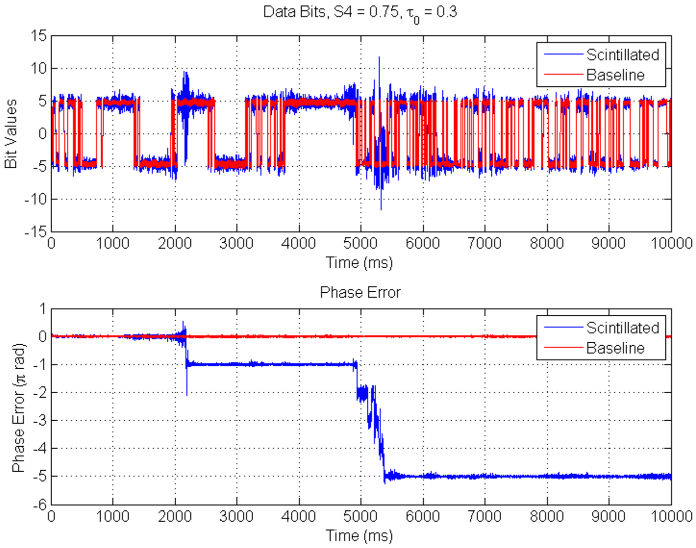

Figure 2.18: Cycle slip example demonstrating successful tracking. Top plot shows data bit values, bottom plot shows corresponding PLL phase error. Scintillated data is shown in blue, baseline (clean) data is shown in red.

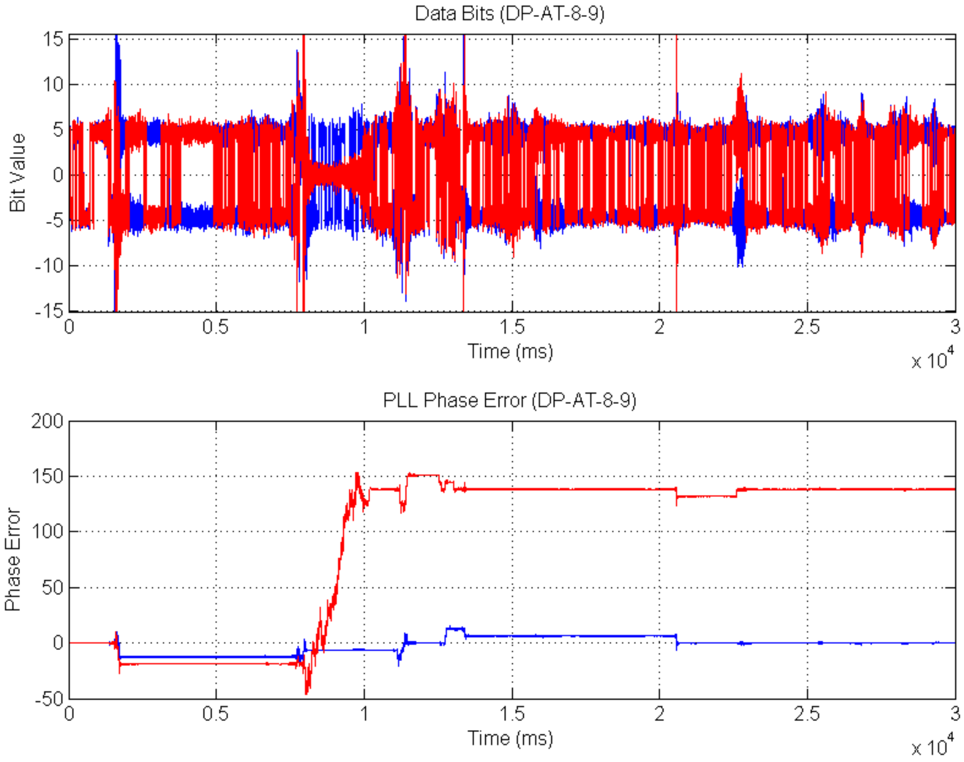

Figure 2.19: Cycle slip example demonstrating bit rotation and temporary loss-of-lock. Top plot shows data bit values, bottom plot shows corresponding PLL phase error. Scintillated data is shown in red, baseline (clean) data is shown in blue.

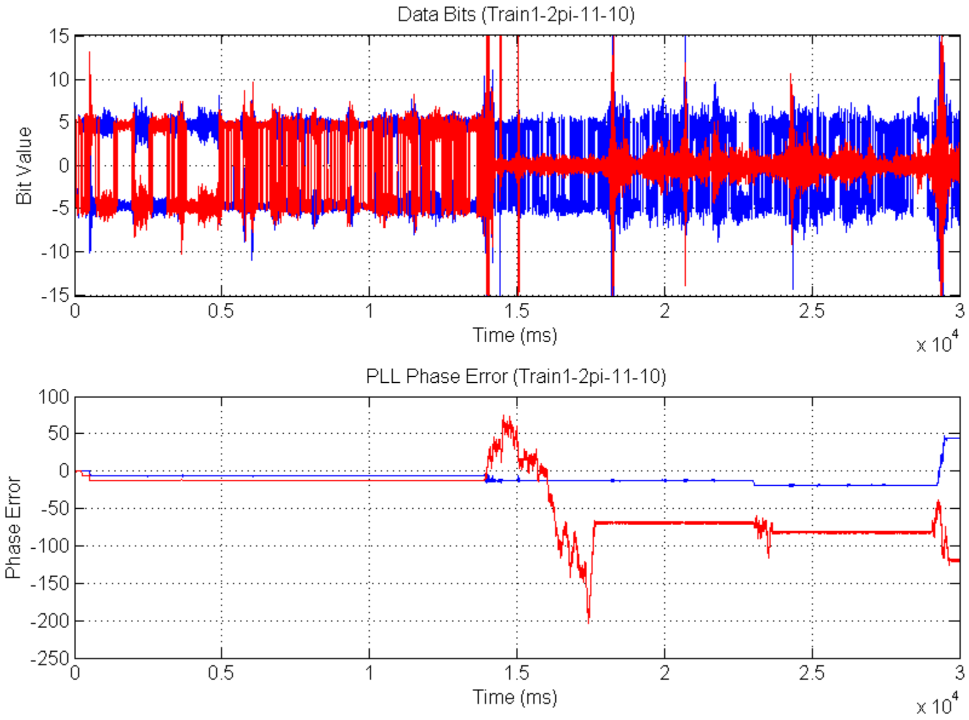

Figure 2.20: Cycle slip example demonstrating complete loss-of-lock. Top plot shows data bit values, bottom plot shows corresponding PLL phase error. Scintillated data is shown in red, baseline (clean) data is shown in blue.

Kinter, et. al. [22] uses an analogy of a picket fence to help visually describe scintillation. Scintillation can be represented by a picket fence sliding through the ionosphere with variable speed, interrupting the GPS signal and producing a signal with time varying amplitude. The signal observed at the receiver will in effect include both the direct line-of-sight signal as well as other interfering diffracted signals. If each of these signals is modeled as a vector with magnitude and phase, the resulting magnitude and phase of the current sample will be the sum of these vectors.

2.3.3 Scintillation Model

Many statistical and theoretical models for scintillation have been developed based on recorded GPS data, scintillation monitors, and observations of space weather and atmospheric activity. This section provides an overview of the current models used in practice.

WBMOD

WBMOD, short for Wide Band Model, is a comprehensive ionospheric scintillation computer model developed at the NorthWest Research Associates (NWRA). Using several user parameters such as location, date, time, and geophysical conditions, WBMod estimates the severity of the scintillation effects based on electron density irregularities, as well as computes the scintillation intensity index, S_4, and phase scintillation index, the rms phase [36]. One of the most important and useful parameters generated by WBMOD is the height-integrated electron-density irregularity strength, otherwise known as C_kL. The C_kL parameter is actually the product of C_k and L, the 1km cross section of the power-spectral density of the ionospheric irregularity and the thickness of the irregularity layer, respectively [35]. C_kL is an alternative representation of the total electron content. The C_kL parameter can be visualized as an estimate of "the total 'power' in the electron density irregularities along a vertical path passing through the entire ionosphere" [36]. It is the most complex parameter created by WBMOD since it is affected by the time of year, local time, location, solar cycle, and geomagnetic activity.

Satellite navigation systems such as GPS are sensitive to small scale irregularities in the ionosphere which can be difficult to model in simulation and are hence omitted from WBMOD. Since WBMOD takes into account large scale irregularities, such as the drift of ionized plasma, this program provides overall realistic results for measures of scintillation when the irregularities are weak to moderate. An experiment conducted by Forte and Radicella ([11]) compared the predicted results of WBMOD to actual scintillation values recorded using a scintillation monitor operated by the Institute of Physics of the National

University of Tucuman in Argentina. Forte and Radicella discovered that the computer model provides poor estimates during periods of high electron density fluctuations (high S_4 indices), which is when GPS receivers are most likely to lose signal lock.

In summary, WBMOD can provide a rough estimate for scintillation in a given area however it lacks precision and resolution which makes it unreliable for predicting scintillation indices for a GPS link. Based on the comparisons made, "the use of scintillation models to estimate ionospheric scintillation effects on single GPS links and thus on GPS operations does not appear to be feasible" [11].

Statistical Model

Various statistical models have been designed to more precisely estimate ionospheric scintillation. In [45] the scintillation fading channel coefficient $\alpha_{sc}(t)$ is modeled as a non-zero mean complex Gaussian random process:

$$\alpha_{sc}(t) = \alpha_{sc} e^{j\phi} + n_{sc}(t), \tag{2.4}$$

where α_{sc}^2 is the received signal power, ϕ is a phase shift uniformly distributed on $[-\pi, \pi]$, and $n_{sc}(t)$ represents the scintillation-induced fading modeled as a complex Gaussian random process. $n_{sc}(t)$ has an autocorrelation function represented by:

$$R_{sc}(\tau) = 2\sigma_{sc}^2 \cdot e^{-(\tau/\tau_0)^2}, \tag{2.5}$$

where σ_{sc}^2 is the power of the scintillation-induced multipath reflections and τ_0 is the signal decorrelation time. τ_0 is defined as the time lag in which the auto correlation function of a scintilled signal is reduced by a factor of $1/e$. The amplitude coefficient distribution is characterized by the PDF of a Rician fading channel; [13] verifies that this is a good fit by comparing Rician and Nakagami-m distributions to empirical data, as shown in Figure 2.21, found in [13, pp. 3].

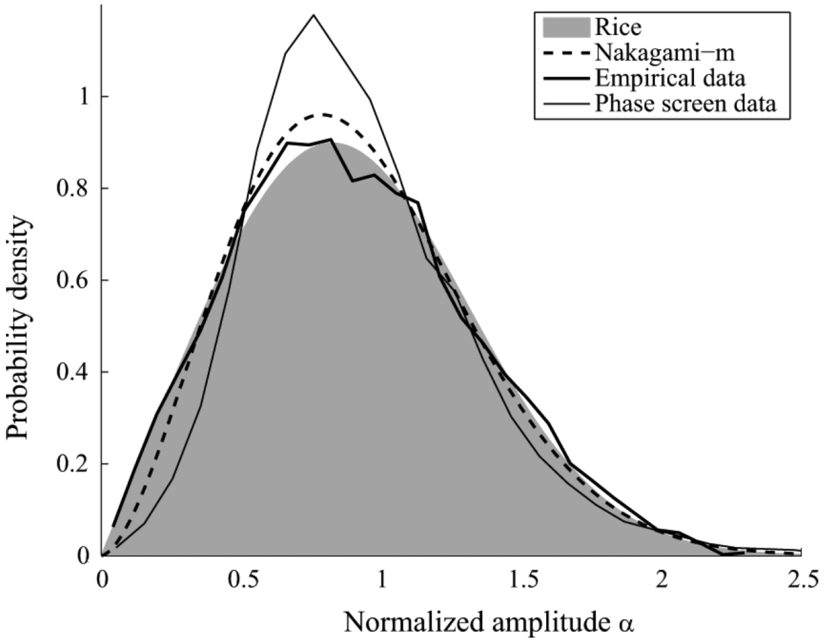

Figure 2.21: A comparison of the Rician and Nakagami-m amplitude distributions to empirical data, retrieved from [13, pp. 3]

Although this model accurately characterizes the fading channels induced by scintillation and multipath, it does not account for phase rotations that occur during canonical fades. [14] builds upon these models but is designed specifically to model the canonical fades that are most typically responsible for bit errors and cycle slips.

Statistical Model Derived Empirically

Unlike the model presented by [45] in which the phase error ϕ is uniformly distributed on $[-\pi : \pi]$, [14] explores a model with phase error that is dependent on the intensity of the fading channel. The phase error variance σ_ϕ^2 is represented by:

$$\sigma_\phi^2 = \frac{B_n N_0}{C}, \tag{2.6}$$

where B_n is the PLL noise bandwidth and C/N_0 is the carrier to noise density ratio. Although this modification to the model correlates the phase error to the fading channel it assumes the PLL operates linearly. However during periods of strong scintillation and canonical fading, phase errors are time correlated and the PLL can not be expected to operate linearly [14].

Due to the nonlinear properties of the PLL during strong scintillation, the model relies on deriving a statistical model based on observations of empirical data collected during periods of varying scintillation intensity. The scintillation library includes a collection of UHF and L-band wideband data from the DNA Wideband satellite experiment from 1976-1979 recorded on the Kwajalein Atoll in the Marshall Islands and Ancon, Peru, as well as GPS L1 data recorded at Cachoeira Paulista, Brazil. The wideband data set was chosen because of the wide range of scintillation intensity (S4 intensities ranging from 0 to 1.2) and because much of the transmissions are coincident with the GPS L-band frequency range [15].

Using the empirical data library, [14] establishes relationships between the S4 index; C/N_0, the nominal carrier to noise density ratio; σ_ϕ, the standard deviation of the phase error; the mean time between cycle slips; and the bit error rate. The original autocorrelation function, $R_{sc}(\tau)$ is replaced by a second-order Butterworth filter represented by:

$$R_{sc}(\tau) = \sigma_{sc}^2 \cdot e^{-\beta|\tau|/\tau_0} \cdot \{cos(\frac{\beta\tau}{\tau_0}) + sin(\frac{\beta\tau}{\tau_0})\}, \tag{2.7}$$

where $\beta = 1.2396464$ was selected to satisfy $R_{sc}(\tau_0) = e^{-1}$, the definition of the decorrelation time τ_0. σ_{sc}^2 is related to K, the Rician K-parameter by:

$$\sigma_{sc}^2 = \frac{1}{2(1+K)}, \tag{2.8a}$$

where K is modeled by:

$$K = \frac{\sqrt{1-S_4^2}}{1-\sqrt{1-S_4^2}}, S_4 \leq 1. \tag{2.8b}$$

A selection of these results will be discussed in the following sections as they pertain to this thesis. In summary, the scintillation model can be fully characterized by the S4 index, the measure of the scintillation intensity, τ_0, the speed of the fluctuations, and C/N_0, the signal's nominal carrier to noise density ratio.

Scintillation Testbed

Ionospheric scintillation is a rare event, one that primarily occurs during periods of heightened solar activity such as during the solar maximum which occurs every 11 years. Due to the sporadic nature of scintillation opportunities for testing receiver algorithms and designs are very limited. Thus to effectively test performance of GPS receivers under scintillation conditions, an accurate scintillation model is necessary. The scintillation testbed devised in [13] (described in the previous section) is the one utilized in this thesis to evaluate the performance of various PLL tracking loops.

The scintillation testbed is implemented in Matlab and generates a complex scintillation vector representing amplitude and phase based on input S4 and τ_0 parameters. In addition the model exports parameters to certain RF signal generators that add scintillation to the transmitted GPS signal. Due to limitations of the GPS signal generator used in this thesis (Pendulum GSG-55), the scintillation model was modified to add scintillation to the received IF signal, as will be described in the following chapter.

2.4 Tracking Methods and Performance

Scintillation poses a problem for GPS receivers because the resulting signal phase and amplitude fluctuations causes carrier recovery to lose lock and hence tracking to fail. This section provides details on the operation of the carrier tracking loops, explains how the effects of scintillation negatively impact tracking performance, and discusses existing carrier recovery algorithm designs.

2.4.1 Traditional PLL

Carrier recovery requires use of a phase locked loop (PLL). The purpose of a PLL is to control the generation of a carrier replica with the same phase as the carrier of the transmitted signal, or in other words, a replica with phase locked to that of the carrier. PLLs can be classified as non-squaring or squaring. A traditional PLL is non-squaring meaning it is sensitive to 180 degree (π radian) phase rotations, and hence BPSK bit transitions.

A traditional PLL operates by minimizing the phase error difference between the original and replica carrier. For example, Figure 2.22a shows a BPSK constellation diagram experiencing counter-clockwise phase rotation. The blue and red circles indicate the ideal positions of the bit values of 1 and -1, respectively, and the blue and red 'X's indicate the in-phase and quadrature coordinates of the actual received bit values of 1 and -1, respectively. The arrows indicate the direction of phase progression. In this case, the PLL discriminator would generate phase errors corresponding to each received bit's error, ϕ, as denoted in blue and red in Figure 2.22b.

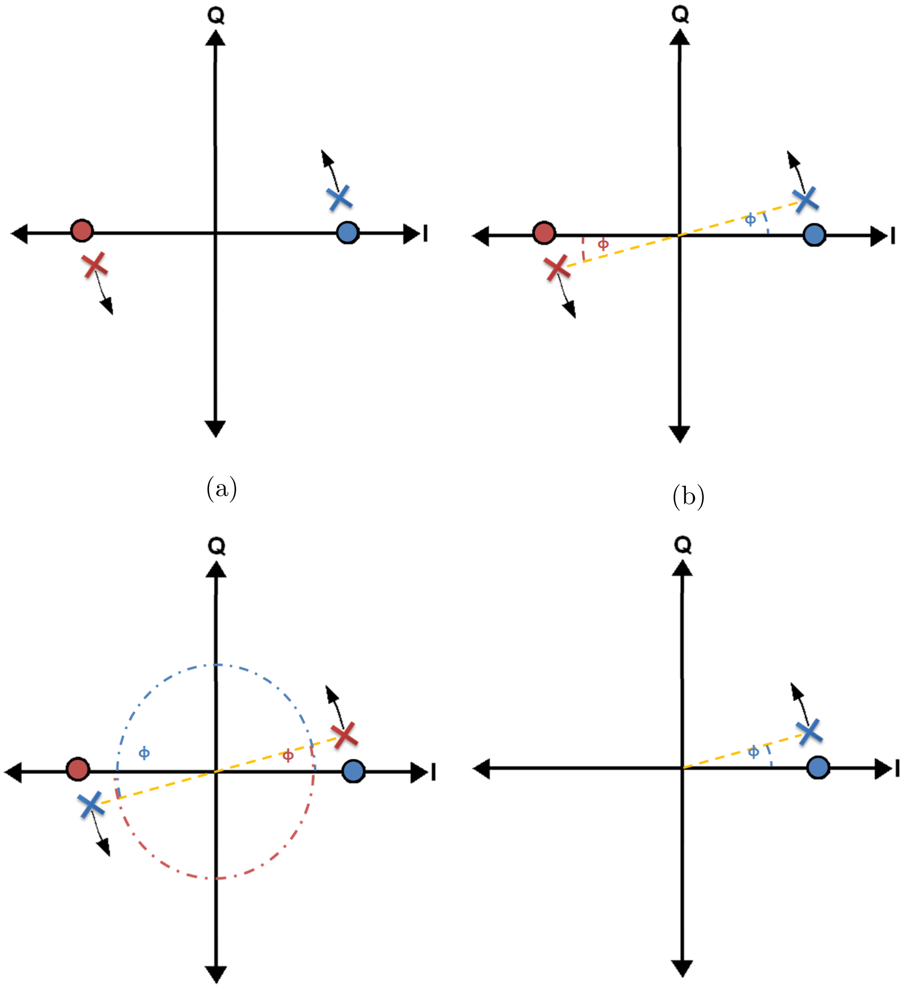

(a) (b)

(c) (d)

Figure 2.22: BPSK Constellations. BPSK constellation showing counter-clockwise (CCW) phase rotation (a), BPSK constellation showing phase error between the expected and the received bit values (b), BPSK constellation showing phase error and π ambiguity resulting from a bit transition (c), and BPSK constellation after data wipe-off (d).

BPSK signals have a 180 degree phase rotation every bit transition. Suppose the bit value changed from a 1 to a -1, as denoted by the 180 degree rotation of the 'X's in Figure

2.22c. In this scenario, the PLL discriminator computes a phase error that is actually off by π:

$$\phi_{Actual} = \phi_{Computed} + \pi. \tag{2.9}$$

To correct for this phase ambiguity, traditional PLL algorithms require an additional step known as data wipe-off [21]. Data wipe-off uses known data (such as training data) or some means of estimating the data bits to remove data from the baseband signal leaving just the carrier. Regardless of the data bit, the baseband signal passed to the PLL discriminator would have a constellation similar to that of Figure 2.22d in that the in-phase component of all bits is roughly the same. A common discriminator for the traditional PLL is the 4-Quadrant arctangent function with phase error given by:

$$\phi_E = \mathrm{ATAN2}(Q_P, I_P) \tag{2.10}$$

where Q_P and I_P are the quadrature and in-phase prompt correlator outputs, respectively and ATAN2 is the 4-Quadrant arctangent function [6]. Without data wipe-off, this non-squaring discriminator is sensitive to phase changes (bit transitions) because output values exist for $\phi_E \in [-\pi, \pi]$.

Two data wipe-off schemes were explored in [14] that are designed to operate with the ATAN2 discriminator. A decision-directed four-quadrant arctangent (DDAT) discriminator achieve data wipe-off by estimating the current bit value using $\mathrm{sign}(I_{P,k})$ where $I_{P,k}$ is the sum of the prompt correlator outputs up to sample time t_P of the current (kth) bit. The discriminator is modeled by:

$$\phi_E = \mathrm{ATAN2}(Q_P \cdot \mathrm{sign}(I_{P,k}), I_P \cdot \mathrm{sign}(I_{P,k})). \tag{2.11}$$

The second method, a dot-product four-quadrant arctangent (DPAT) discriminator utilizes differential bit detection. Data wipe-off is achieved under the assumption that on average data symbols will change every two bits, or 40 ms [9]. The data bit estimate is computed by taking the dot product of the phase of the current and previous bits. The discriminator is modeled by:

$$\phi_E = \mathrm{ATAN2}(Q_P \cdot d_{P,k}, I_P \cdot d_{P,k}), \tag{2.12a}$$

where $d_{P,k}$ is the estimate of the current bit value and computed by:

$$d_{P,k} = \begin{cases} -d_{k-1} & \mathrm{Re}\{(\sum_{\substack{m\mathrm{th} \\ bit}} I_{P,k} - jQ_{P,k}) \cdot (\sum_{\substack{m-1\mathrm{th} \\ bit}} I_{P-1,k} + jQ_{P-1,k})\} < 0 \\ d_{k-1} & \mathrm{Re}\{(\sum_{\substack{m\mathrm{th} \\ bit}} I_{P,k} - jQ_{P,k}) \cdot (\sum_{\substack{m-1\mathrm{th} \\ bit}} I_{P-1,k} + jQ_{P-1,k})\} \geq 0. \end{cases} \tag{2.12b}$$

In the event the dot product of the phase differences are approximately zero, the DPAT discriminator reverts back to the DDAT model.

2.4.2 Costas Loop

A squaring PLL, also referred to as a Costas loop, is a less complex PLL model that is insensitive to 180 degree (π radian) phase rotations resulting from bit transitions. This property makes Costas loops a common choice for GPS carrier recovery schemes. The Conventional Costas discriminator is a popular choice for GPS receivers because it is near optimal at low SNR. Its phase error is computed by

$$\phi_E = \frac{\mathrm{ASIN}(Q_P \cdot I_P)}{2} \tag{2.13}$$

Another common Costas loop discriminator is the 2-Quadrant arctangent function with phase error given by:

$$\phi_E = \mathrm{ATAN}(Q_P / I_P), \tag{2.14}$$

where Q_P and I_P are the quadrature and in-phase prompt correlator outputs, respectively and ATAN is the 2-Quadrant arctangent function [6]. This discriminator is suboptimal but provides robust performance at both high and low SNR. Outputs of both discriminators only exist in the range $\phi_E \in [-\pi/2, \pi/2]$. Referring back to Figure 2.22b, a Costas loop can generate a phase error regardless of the data bit transmitted because the error is computed with respect to the in-phase (horizontal) axis. There are no π radian phase ambiguities for this discriminator.

2.4.3 Variable-Bandwidth PLL

A complex alternative to the conventional Costas and variations of the traditional PLL is a variable-bandwidth PLL such as the Kalman Filter PLL (KFPLL). The noise bandwidth of the PLL's filter determines the robustness of the carrier tracking algorithm. Larger noise bandwidths can tolerate more stress, such as rapid phase changes induced by scintillation; however smaller bandwidths will improve accuracy [21]. The noise bandwidth is generally fixed, however [43] suggests a PLL with either larger or variable bandwidth could prove beneficial:

> Generally, the scintillation induces excess carrier phase jitter in the phase lock loop (PLL) of the GPS receiver, and strong scintillation can cause a conventional PLL (ATAN [arctangent method], constant bandwidth Bn = 10 Hz) to lose phase lock resulting in no GNSS signal available at that time from the satellite path(s) affected. A PLL with a larger bandwidth is one solution to mitigate this but at the expense of extra phase noise, and this may not be an optimal solution during weak scintillation conditions. [43]

Humphreys, et. al. [14] explores the possibility of a KFPLL. Although the KFPLL is well suited to avoid frequency unlock, its cycle slip rate fares poorly compared to the PLLs utilizing data wipe-off methods. The degrade in performance is attributed to the KFPLL's inability to quickly adapt to scintillation's rapid phase changes. Therefore variable-bandwidth PLLs will not be further discussed in this thesis.

2.4.4 Discriminator Performance

In the absence of scintillation, decision-directed ($\phi_E = Q_P \cdot$ sign$(I_{P,k})$) and Conventional Costas ($\phi_E = I_P \cdot Q_P$) performed the best. Compared to the DDAT discriminator, the mean time between cycle slips for the Conventional Costas were approximately an order of magnitude greater, and for the decision-directed were approximately two orders of magnitude greater. The DPAT yielded the worst performance with time between cycle slips up to three orders of magnitude less than the DDAT model. Figure 2.23 shows the empirical results of the experiment.

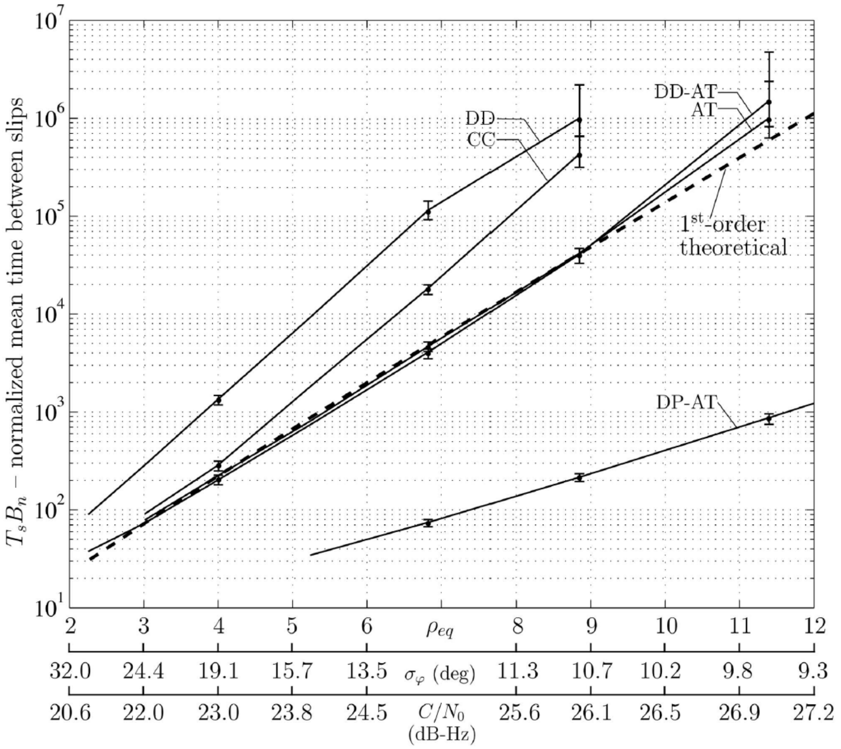

Figure 2.23: Experimental cycle slip performance of various PLL discriminators, retrieved from [14, pp. 6].

After scintillation is added to the GPS signal, the results are nearly reversed in that the DPAT discriminator yields the highest mean time between cycle slips, followed closely by DDAT. Figure 2.24 shows a comparison of various tracking techniques for UHF Wideband data suffering strong scintillation (S4 > 0.6).

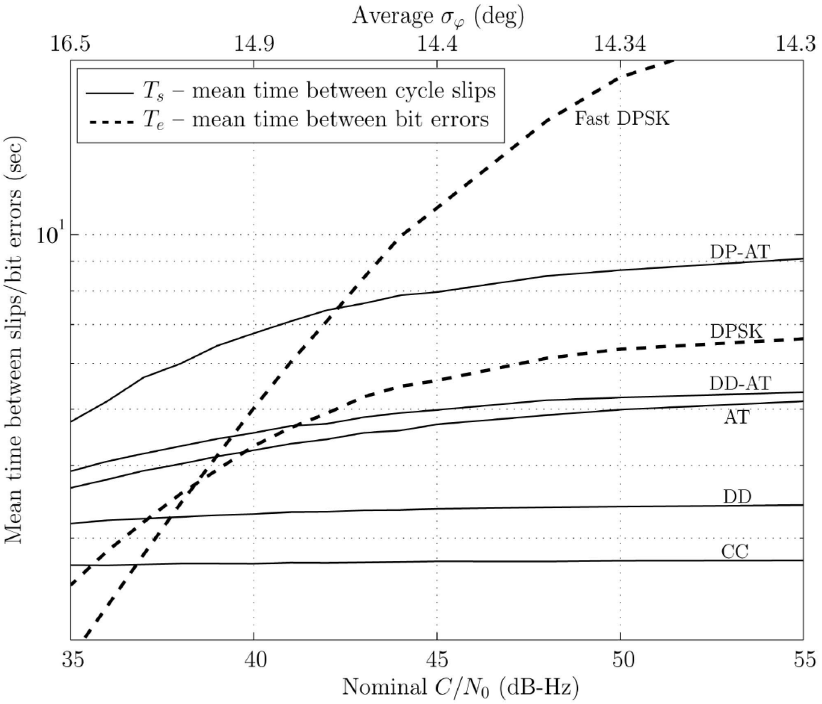

Figure 2.24: Experimental cycle slip and bit error performance of UHF Wideband data operating in strong scintillation using tracking techniques, retrieved from [14, pp. 8].

There are a few important notes about this figure. First, UHF Wideband data, not GPS data, was used to characterize the performance of each tracking technique due to more data and a wider variety of data available. Second this figure provides, for comparison, bit error rates of differential PSK (DPSK) demodulation. The use of DPSK in [14] was primarily to establish a relationship between cycle slipping and bit error rates. Although using DPSK shows improved performance for this scenario, this thesis focuses primarily on improving the performance of carrier recovery loops during ionospheric scintillation. Additionally because DPSK schemes are not robust enough to provide improved performance under normal tracking conditions (i.e. in the absence of ionospheric scintillation), DPSK demodulation schemes are omitted from this thesis.

Two additional figures included in the study provide insight into the relationship between the cycle slip rates, the standard deviation of the PLL phase error, and the bit error rates. Both of these relationships were used to help improve the characterization of ionospheric scintillation in order to develop the model utilized for testing in this thesis. The relationship between cycle slip rate and S4 shown in Figure 2.25 reveals that high cycle slip rates are frequent for S4 indices exceeding 0.6. The mean time between cycle slips for DDAT and DPAT are about 37s and 43s, respectively.

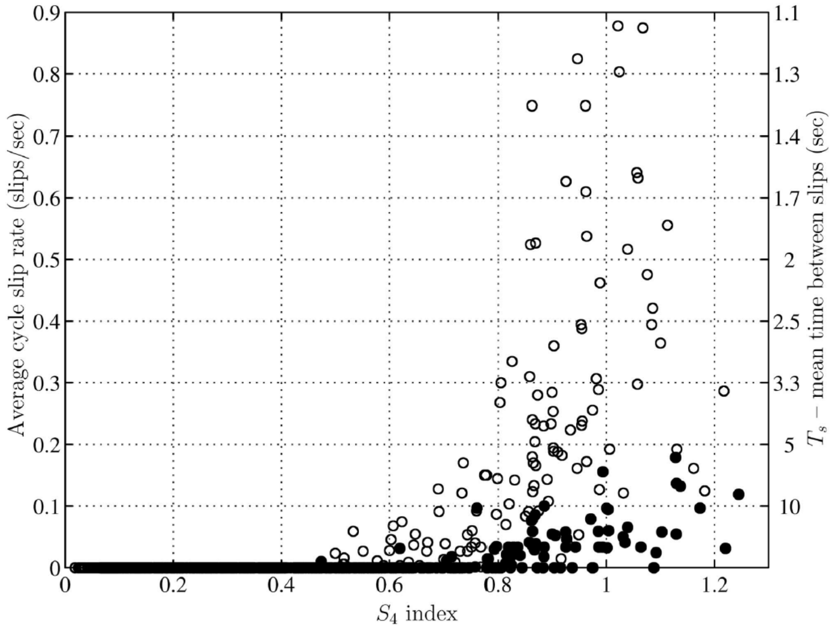

Figure 2.25: Mean cycle slip rate vs S4 for wideband data (open circles) and GPS L1 data (closed circles) both with nominal $C/N_0 = 43$ dB-Hz. Carrier recovery utilizes a DD-AT discriminator. Plot retrieved from [14, pp. 7].

Figure 2.26 is useful for showing the relationship between the cycle slip rate and the bit error rate (BER). There is a linear relationship, nearly 1-to-1 mapping, between the two parameters. This correlation is important because it shows that both mean time between cycle slips and the BER are good measures of PLL performance.

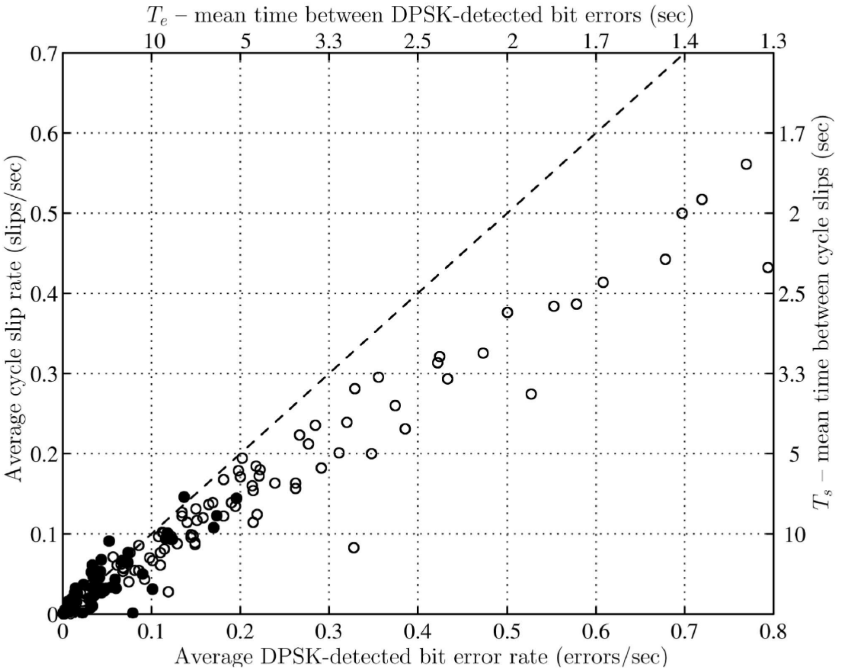

Figure 2.26: Mean cycle slip rate vs DPSK detected bit errors for wideband data (open circles) and GPS L1 data (closed circles) both with nominal $C/N_0 = 43$ dB-Hz. Carrier recovery utilizes a DP-AT discriminator. Plot retrieved from [14, pp. 10].

2.5 Chapter Summary

GPS data transmissions are structured using frames and subframes. The first three subframes include clock corrections, information on the satellite vehicle, and ephemeris parameters, which describe the satellite's orbit and current position in space. These three subframes repeat with every new frame (every 30 seconds) and comprise nearly 60 percent of a GPS frame. The high rate of repetition and low update rate shows that these subframes can potentially be used as training data for future samples acquired during periods of scintillation.

Ionospheric scintillation is a phenomenon that is caused by a changing refractive index created by charged particles in the ionosphere; periods of scintillation often accompany and are the result of solar storms. Scintillation results in simultaneous deep fades and rapid phase shifts in the GPS signal. This combination makes it especially difficult to sustain tracking because the PLL suffers cycle slips which degrades the carrier frequency estimate. Long periods of cycle slipping (up to several seconds) can result in total loss of lock. At this point, reacquisition may be necessary to regain tracking.

GPS receivers utilize phase locked loops to maintain lock on the carrier frequency and sustain tracking of the GPS signal. Due to the BPSK modulation scheme, the Costas loop is a common carrier recovery technique because it is insensitive to pi radian phase rotations (bit transitions). Under normal operating conditions, this algorithm has a high success rate. However, the current state of the art in receiver design mitigates scintillation by using a PLL discriminator that can detect up to pi radian phase rotations. Four-quadrant arctangent, decision-directed methods improve the range of error detection and experimental results show improved tracking performance compared to the Costas algorithm. As a result, algorithms that will be explored in the following chapter will be based upon this four-quadrant arctangent, decision-directed architecture.

Chapter 3

Implementation

The purpose of this chapter is to discuss the implementation of the scintillation GPS receiver testbed. First, an overview of the hardware components will be provided, including the GPS signal generator and RF front-end. Next the software components will be discussed which include the GPS processing scripts and scintillation testbed. Finally this chapter will discuss the theory and implementation of various receiver models that are tested. The following chapter will explain the experiments and results of each method.

The hardware components used to build the testbed include the Pendulum GSG-55 GPS signal generator and the Universal Software Radio Periferal (USRP) software radio. The software components include GPS processing scripts, a scintillation testbed, and performance verification all of which are implemented in Matlab. A high-level block diagram of the implementation is presented in Figure 3.1.

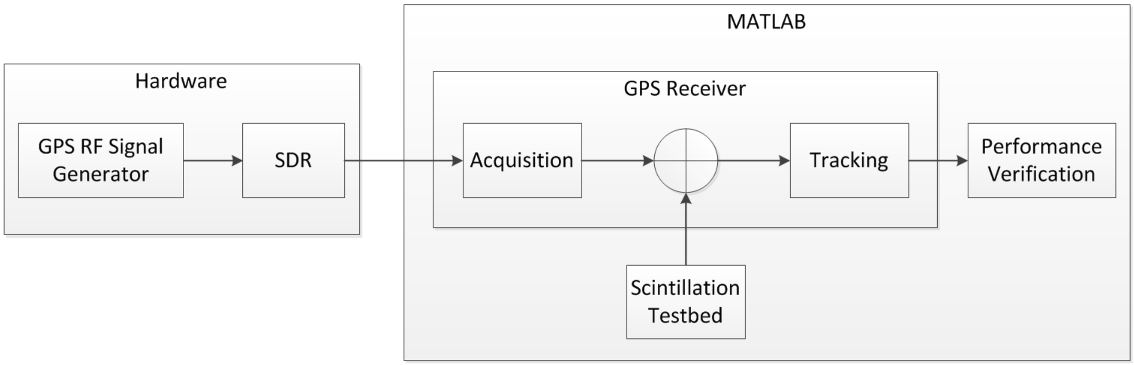

Figure 3.1: High-level block diagram of the GPS testbed implemented in this thesis

3.1 Hardware and Software Components

3.1.1 GPS Signal Generator

The GPS signal generator used in this testbed is the Pendulum GSG-55. The GSG-55 is an RF L1 GNSS (GPS and GLONASS) signal generator capable of simultaneously transmitting up to 16 different channels at power levels of -160 dBm to -65 dBm. The user has complete control over date and time of transmission, transmission power levels, additive noise channels, as well as location and direction of movement of the receiver (stationary receivers are also an option).

3.1.2 Software Radio

The software radio used is the Universal Software Radio Peripheral (USRP). The USRP is a readily reconfigurable radio platform that can transmit and receive over a wide range of frequencies, depending on the RF daughtercard selected. The USRP supports clock synchronization via a 10 MHz reference and 1 peak-per-second (PPS) inputs. The radio interfaces with a computer via a gigabit-Ethernet connection; the open source program GNU Radio Companion (GRC) is used for controlling and acquiring data samples from the radio.

There are actually two different USRP models, the USRP2 and newer USRPN210. The two radio models are shown in Figures 3.2a and 3.2b, respectively. The USRP2 was originally used but due to poor performance, particularly a high noise floor, the USRPN210 model was chosen for implementation in the final design. Figure 3.3 shows a comparison of the power spectral densities for the USRP2 and N210 models using a GPS signal transmitted at -65 dBm and 10 MHz receive bandwidth. As shown, the N210 model has about 13 dB more gain than the USRP2. The peak of the two signals is approximately centered at the intermediate frequency of 1.5 MHz. The reason why the two PSDs do not line up exactly is because a frequency offset exists between the two local oscillators; this offset can be corrected for in the software processing.

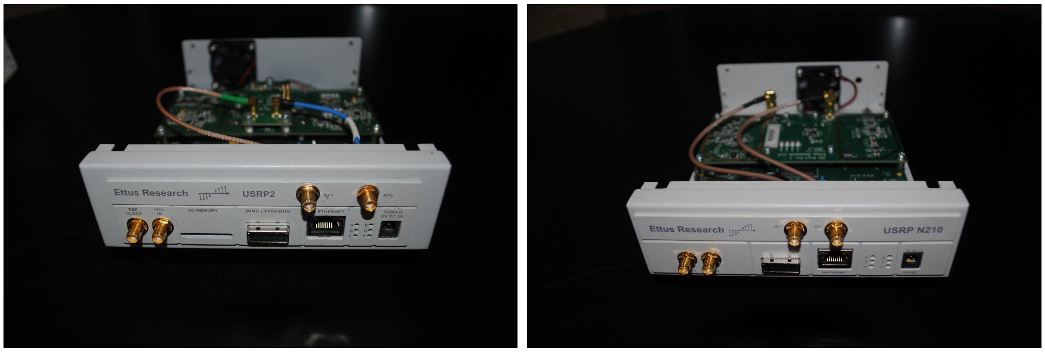

(a) (b)

Figure 3.2: Universal Software Radio Peripheral: USRP2 (a) and newer model USRP N210 (b).

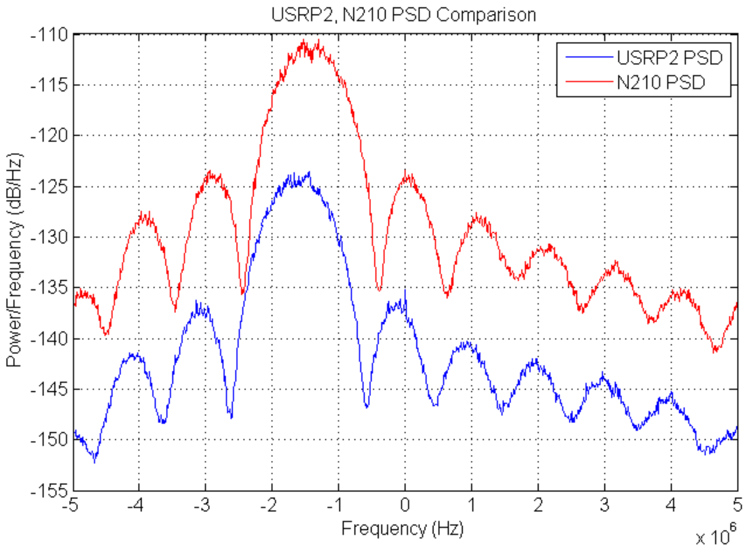

Figure 3.3: A comparison of the PSDs for the USRP2 (blue) and USRPN210 (red) for a transmit power of -65 dBm and receive bandwidth of 10 MHz. The N210 has about 13 dB of gain compared to the USRP2.

The front end of the USRP is not sensitive enough to detect very low powered signals such as GPS. Based on experimentation, a lower bound of approximately -90 dBm was found to be the threshold for successful reception and demodulation of GPS signals. Figure 3.4 shows a comparison of PSDs generated using the USRP2 receiving four different power levels. After -90 dBm, the signal spectrum (centered at IF = 1.5 MHz) is nearly lost in the noise.

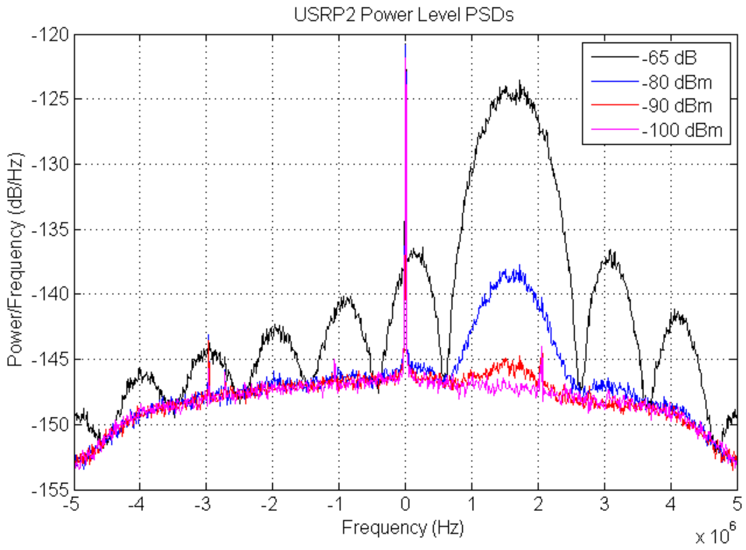

Figure 3.4: A comparison of the USRP2 PSDs for different transmit power levels.

The USRP is a highly versatile platform in part because it supports many different interchangeable RF frontends known as daughtercards. Each daughtercard supports different features and operates in a specific frequency range. The SBX daughtercard was chosen for this project because it operates in the range of 400-4400 MHz which includes GPS L-band frequencies.

3.1.3 GNU Radio

GNU Radio Companion (GRC) is an open source program that is used to interface with the USRP via a gigabit ethernet connection. GRC allows the user to control the center frequency and sampling rate of the USRP as well as interact with and record raw RF samples. For example, GNU Radio supports various signal processing functions such as filters, FFTs, and demodulation schemes. Since all of the GPS processing is conducted offline in Matlab, GRC is primarily used for recording raw data samples.

3.1.4 GPS Software

The GPS processing program, SoftGNSS v3.0, is open-source software written by Darius Plausinaitis and Dennis M. Akos, and accompanies [6]. The program is a collection of Matlab scripts that are built modularly to achieve acquisition, tracking, and navigation processing. The scripts were originally designed to operate with the SiGe GN3S GPS sampler. This RF frontend operates at a different IF and records data differently than the USRP; however only minor adjustments to the code were necessary to interface the two.

3.1.5 Scintillation Testbed

The Cornell Scintillation Simulation Toolkit, written by Todd Humphreys, is based on the models derived and verified in [13], [14], and [15]. This scintillation model was chosen for this thesis because it is designed to accurately generate a scintillation channel containing the canonical fades that are generally responsible for carrier tracking errors and loss of frequency lock. Furthermore this model is implemented in Matlab which simplifies implementation with the GPS receiver.

This testbed is designed to export the scintillation parameters to a Spirent GPS signal generator where scintillation of the GPS signal occurs before the RF transmission. Because the Pendulum GSG-55 used does not support this feature, the testbed was modified to support adding the scintillation channel to the raw IF signal after it had been recorded. Although it is not ideal to add the scintillation channel after the signal has been recorded, a comparison between the testbed's input S4 indices and the computed S4 index of the actual signal show this method is acceptable for implementation. More details on scintillation implementation will be discussed in the following section.

3.2 Testbed Implementation

This section explains how all of these components operate together to form a coherent testbed. Add some more introductory type stuff here.

3.2.1 Transmitted Signal

In order to focus solely on the effects caused by scintillation, all controllable variables are held constant. All simulated noise channels are disabled, the GPS RF signal generator uses a high transmit power, and the output is connected directly to the software radio using coaxial cable. A 10 MHz reference clock and 1 pulse per second (PPS) signals are used to synchronize the software radio to the GPS signal generator; this ensures that all phase offsets present in the receiver are a result of the additive scintillation channel. Additionally it produces a near-ideal baseline data set that can be used to characterize performance of the receiver. Finally the same 30s raw IF recording is reused for each iteration of the simulation; 30s was selected because one GPS frame is 30s long. This setup is summarized in Figure 3.5.

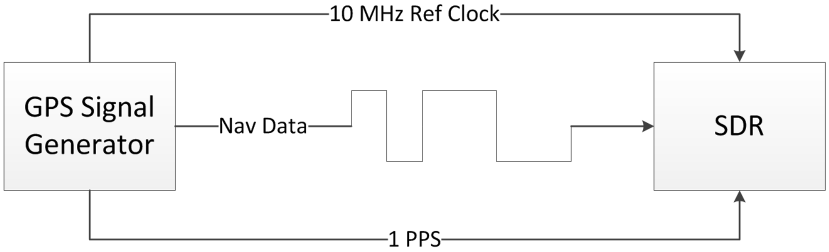

Figure 3.5: Signal transmission block diagram depicting paths of the navigation data and reference clocks.

Actual GPS signals are transmitted at -130 dBm. Ambient thermal noise power spectral density is -174 dBm/Hz. Thus the difference yields a nominal carrier to noise density ratio of 44 dB-Hz. Due to limitations of the RF front-end, the software radio used in this testbed is not able to receive such low powered signals. To account for the poor equipment, the maximum transmit power of the GSG-55 of -65 dBm is used. Using a high transmit power improves the SNR which makes the signal simple to demodulate and provides a high confidence that the received navigation data is actually correct. Correct baseline data is critical for comparing and measuring performance of different receiver models.

When actually testing different receiver models, to use such a high transmit power would be unrealistic. To compensate for the additional power, a simulated noise floor is superimposed on the signal. The power of this additive white Gaussian noise (AWGN) channel is selected such that the ratio of the noise power spectral density to the signal power (-65 dBm) is the same as for an actual GPS signal. For a nominal CN0 of 44 dB-Hz, the power density of the AGWN channel is -109 dB/Hz. When the CN0 increases or decreases due to the fading channel created by scintillation, the amplitude of the AWGN channel is modified accordingly. Using the same noise channel to replicate both nominal and scintillated conditions greatly simplifies the procedure. Implementation of the noise channel will be further discussed in the software section.

3.2.2 Raw RF Recordings

The USRP is unique to many other software radio platforms in that data is exported at complex baseband rather than IF. The RF daughtercards are responsible for demodulating the RF signals to baseband; the FPGA on the USRP then uses a 100 MHz analog to digital converter (ADC) to sample the baseband signal and these complex baseband (in-phase and quadrature) samples are made available to the computer via the gigabit ethernet connection. Although a baseband signal is ultimately desired in order to extract the navigation data, the GPS processing scripts in use expect a signal at an IF. Carrier tracking determines the frequency offset of the IF signal and uses this offset to drive the numerically controlled oscillator (NCO) which updates the frequency of the carrier replica, as shown in Figure 2.10.

GPS signals are transmitted at 1575.42 MHz; thus to demodulate the signal to baseband, the center frequency of the RF front-end would need to be set accordingly to 1575.42 MHz. However this RF signal recorded at baseband may not actually be at baseband. In fact, because the center frequency is constantly changing, the signal may never be exactly at baseband. Carrier recovery corrects these offsets by shifting the signal in the frequency domain through modulation. Using the carrier recovery scheme as-is with a complex baseband signal generated by the USRP will result in aliasing after the corrections are implemented.

A simple solution to fix this aliasing issue is to record the RF signal off-center with a known frequency offset to produce a "pseudo-IF" signal. This pseud-IF signal is really just a complex baseband signal shifted one direction in the frequency domain. Based on the Nyquist sampling theorem, the frequency offset selected must be higher than the highest frequency of the baseband signal. Since GPS has a bandwidth of about 2 MHz, the highest frequency of concern is approximately 1 MHz. A pseudo-IF of 1.5 MHz was selected to provide a buffer of approximately 500 kHz.

Unlike a true IF signal, this pseudo-IF signal has already been separated into its inphase and quadrature components. Since the carrier replica is only used to shift the signal and not to apply a 90 degree phase shift (to extract the quadrature branch), the carrier recovery scheme depicted in Figure 2.10 is modified as shown below in Figure 3.6.

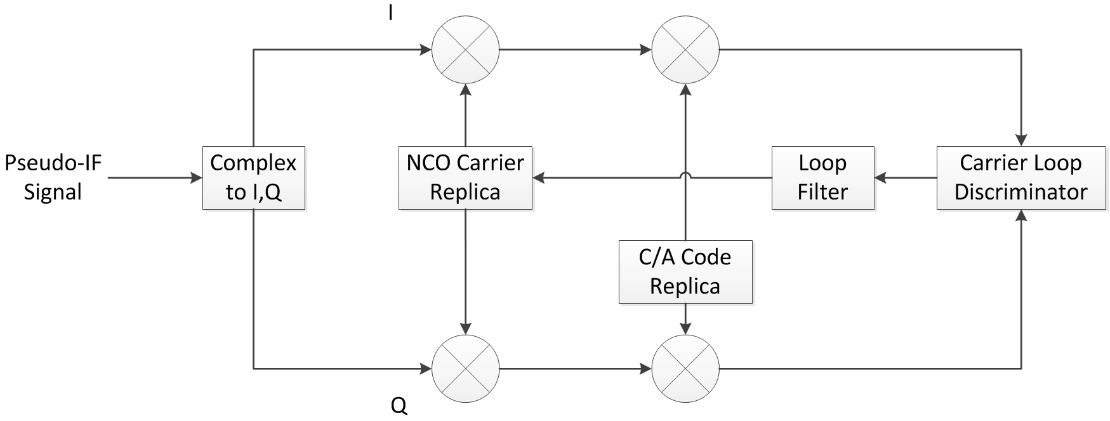

Figure 3.6: Modified carrier recovery block diagram designed to work with an off-center complex baseband signal, otherwise known as a pseudo-IF signal.

3.2.3 Repeating Navigation Data

In an actual GPS signal, the ephemeris parameters and almanac data remain unchanged for up to several hours at a time. Experiments have shown that almanac data over 2 weeks old and ephemeris updated daily can be used to accurately estimate a satellite's orbit [33]. According to the GPS interface specifications [30], there is no clearly defined interval for which these parameters are updated. Despite this ambiguity, the receiver implemented in this thesis assumes that ephemeris data remains consistent for at least several minutes (several frames).

To verify this assumption, several complete (30s long) frames were recorded and the data bits were compared. In the first case the two subframes were recorded sequentially; in the second case, the two subframes were recorded 12.5 minutes apart such that each was from a different navigation message. Using the preamble to align the frames, subframes 1, 2, and 3 were shown to contain the same data bits. Note that this does not include the HOW as this component contains the time of week (TOW) and thus changes between each subframe. The subframe ID was used to verify the same subframes were being compared in each recording. The overlapping data bits for each subframe of two recordings are shown in Figure 3.7.

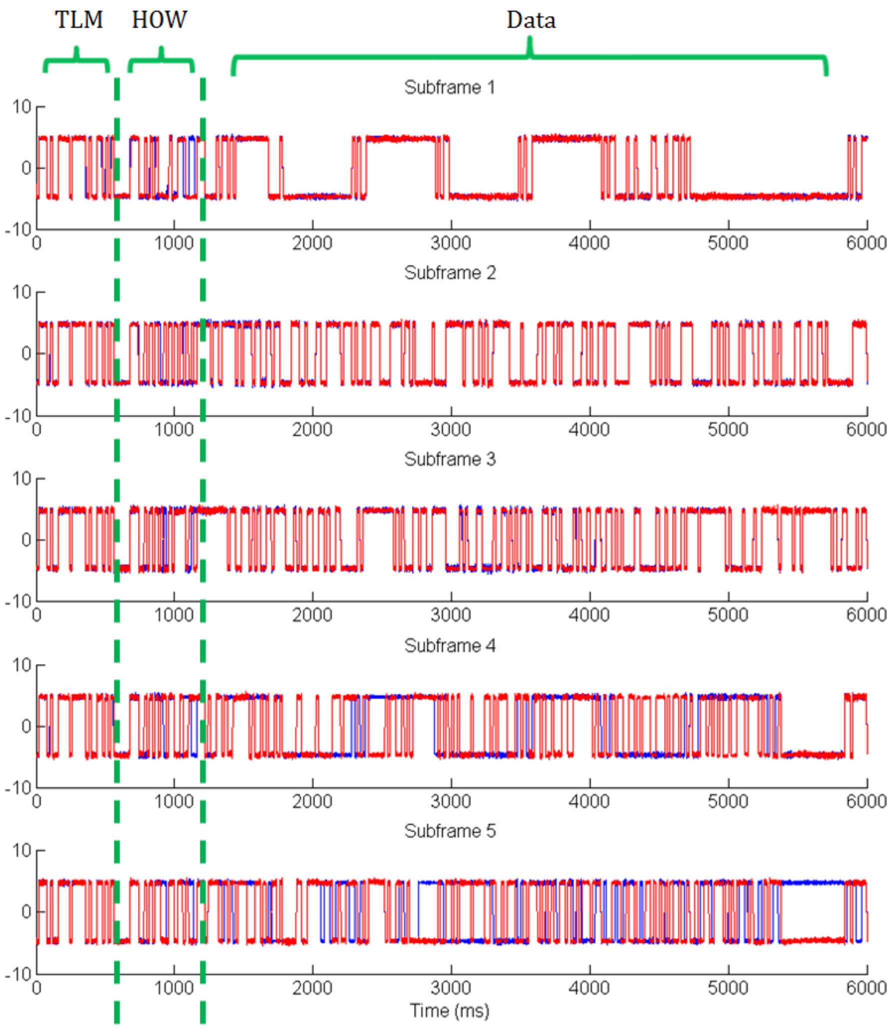

Figure 3.7: Figure showing the data bit overlap for two different frames (one shown in red, one in blue). Green dashed lines separate the TLM, HOW, and navigation data. Each row shows the data for subframes 1-5 with each subframe beginning with the same preamble sequence 10001011. As shown, subframes 1-3 contain identical data (HOW is different), as expected, and the almanac data transmitted in subframes 4-5 is different.

This proof-of-concept experiment shows that nearly 60 percent of the GPS data regularly repeats. Assuming the receiver has accurate timing synchronization, it could be possible to use previously recorded data as a training sequence for upcoming data. The following chapter will show how this repeating navigation data can be exploited to improve carrier recovery compared to existing tracking algorithms.

3.2.4 Adding Scintillation

The scintillation model used in the receiver generates a complex scintillation vector. The angle corresponds to scintillation-induced phase errors (phase scintillation) and the magnitude corresponds to the fading channel (amplitude scintillation). The GPS signal generator is not capable of generating scintillation or rapidly changing the output power. Since there is no way of implementing the scintillation channel before receiving the GPS signal, scintillation must be added to the raw IF signal after it has been recorded.

Amplitude Scintillation As mentioned in Section 3.2.1, the signal generator's transmit power remains constant and is unrealistically high. To compensate, a zero-mean AWGN channel is implemented in software which normalizes the signal power. This AWGN channel is also used to create changes in the carrier to noise density ratio corresponding to the magnitude of the scintillation vector. A block diagram outlining this procedure is shown in Figure 3.8.

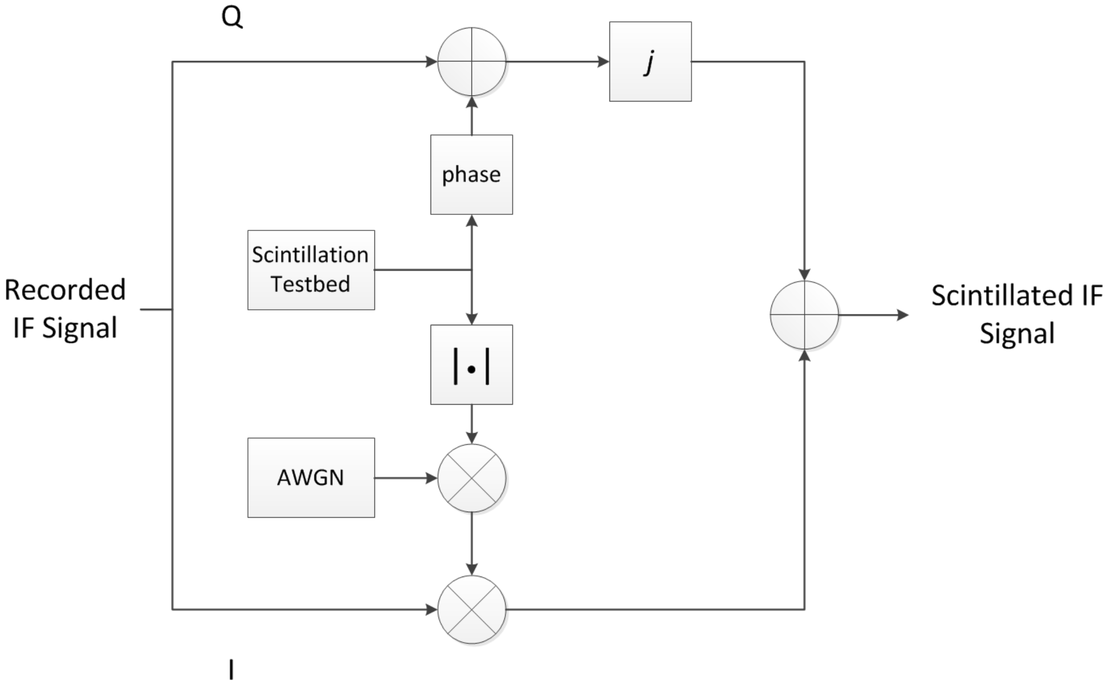

Figure 3.8: Scintillation model block diagram.

The amplitude of the AWGN channel K is determined by the C/N0 value and the power of the signal by:

$$K = 10^{\frac{P_s - C/N0 + BW_{dB}}{20}} \tag{3.1a}$$

where P_s is the signal power in dBm, $C/N0$ is the carrier to noise density ratio in dB-Hz, and BW_{dB} is the receiver bandwidth specified in dB by

$$BW_{dB} = 10 \cdot \log_{10}(BW). \tag{3.1b}$$

The nominal C/N0 value determines the steady-state output of the AWGN channel. This thesis assumes a nominal C/N0 of 44 dB-Hz; for a signal power of -65 dBm, this C/N0 corresponds to a noise density of -109 dB/Hz. C/N0 values generated by the scintillation testbed are used to determine the AWGN channel amplitude when simulating scintillation.

The noise amplitude increases as C/N0 decreases, hence simulating deep fades (amplitude scintillation).

Phase Scintillation The recorded complex IF signal has both magnitude and phase determined by its in-phase and quadrature components. Phase scintillation is implemented by changing the angle of the complex IF signal while maintaining the magnitude. Figure 3.9 provides a graphical representation of how this is accomplished.

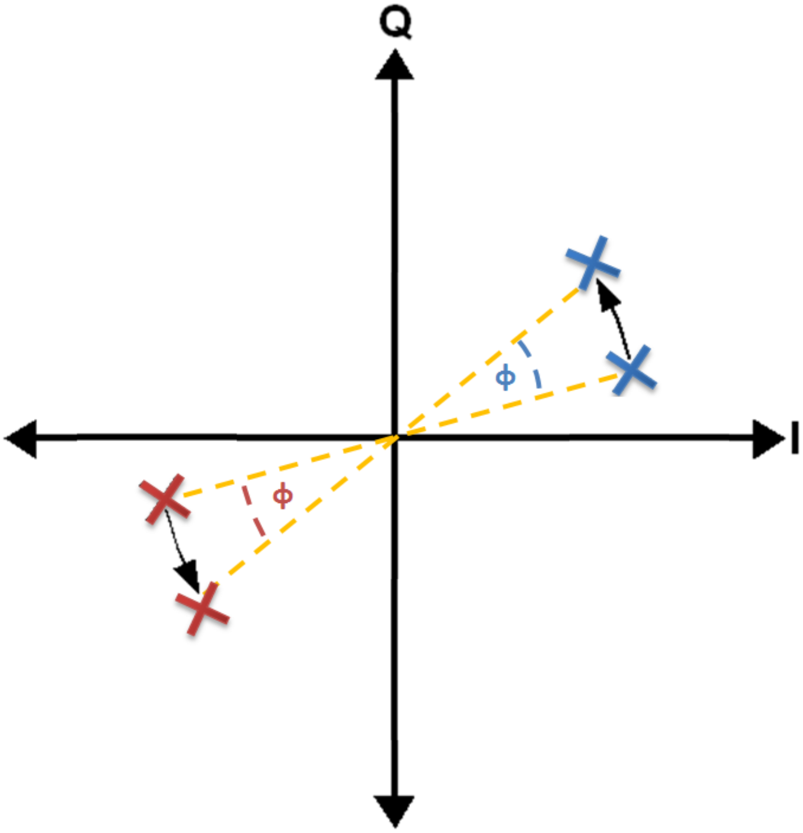

Figure 3.9: Phase scintillation is implemented by rotating the complex IF signal by the angle generated by the scintillation testbed.

In order to maintain the same magnitude when changing the phase, both the in-phase and quadrature components are changed. For example, suppose a bit value 1 is transmitted and scintillation causes a counter-clockwise phase rotation (refer to the blue 'X' in Figure 3.9). The received bit may already have a phase error; the scintillation phase will simply add to this error. To add the error, the in-phase component is decreased and the quadrature component is increased. Mathematically this is achieved by:

$$I_s = |I + jQ| \cdot \cos(\tan^{-1}(\frac{Q}{I}) + \phi_s) \tag{3.2a}$$

$$Q_s = |I + jQ| \cdot \sin(\tan^{-1}(\frac{Q}{I}) + \phi_s) \tag{3.2b}$$

where I and Q are the recorded in-phase and quadrature IF samples, ϕ_s is the phase offset caused by scintillation, and I_s and Q_s are the new (scintillated) in-phase and quadrature IF values, respectively.

Figure 3.10 verifies that this procedure correctly implements the scintillation channel. The graph plots the input scintillation S4 index vs. the empirically computed S4 index using Equation 2.2. Error bars show the standard deviation of the computed S4 value.

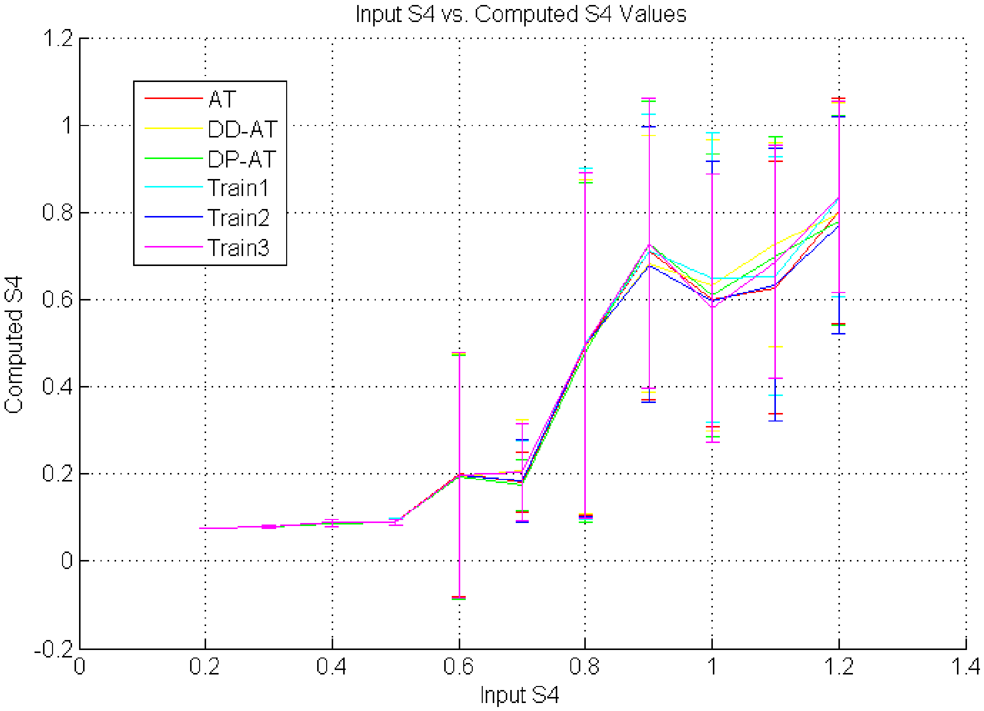

Figure 3.10: Empirical verification of the scintillation testbed implementation.

3.3 Receiver Models

Ionospheric scintillation poses a problem for GPS receivers because bit errors and loss of lock result from degraded carrier tracking performance. Chapter 3 discusses various tracking methods designed to help improve performance. Previous experiments show decision-directed algorithms are more robust in scintillation conditions than conventional Costas and PLLs utilizing arctangent discriminators. All of the decision-directed methods discussed previously rely on no more than the last three bits to determine what the current bit value should be. Because the majority of the GPS signal is repetitive in nature, adding memory to a receiver could enable prior data to serve as a training sequence for future data. This section describes the training-based decision-directed algorithms that are used in this thesis. Experimental results utilizing each of these carrier recovery algorithms will be presented in the following chapter.

3.3.1 Design Specifications

The performance of a phase locked loop is dependent on the accuracy and robustness of the discriminator. The discriminator is the component of the PLL that uses an algorithm to determine the error and return an appropriate correction to the NCO in an attempt to minimize the phase error. If the discriminator can correctly determine the phase error, then the receiver will remain in lock and tracking will continue. Under normal operating conditions (i.e. in the absence of scintillation), phase and amplitude fluctuations are slow and relatively unchanging. As a result the PLL needs to make little compensations to maintain tracking and frequency lock.

In the presence of scintillation however, the environment changes drastically and the PLL now must constantly make rapid phase corrections to compensate for a nonlinear channel. The task of carrier recovery suddenly becomes very demanding and requires a robust discriminator. As studied in [15], near half-cycle phase changes occurring in conjunction with deep fades are the most common causes of cycle slips. In accordance with this property, the first design requirement of the discriminator is it should be able to detect phase errors (phase rotations) up to pi radians. In order to accomplish this task, the discriminator cannot use a conventional Costas implementation which is insensitive (and thus unable to detect) pi radian phase rotations. Therefore an alternative PLL algorithm must be used which requires data wiping. This leads to the second design requirement which is that the discriminator must implement a method that accomplishes data wipe-off while minimizing the quadrature component of the signal.

3.3.2 Discriminator Algorithms

Two different training-based decision-directed algorithms are explored in this thesis and compared to the existing decision directed methods discussed in the previous chapter. Discriminators using training data were implemented using the following procedure:

First a complete frame of raw IF GPS data is recorded. Without adding scintillation, the GPS processing scripts extracts and saves the raw data bits from this signal (I_P and Q_P). This information represents GPS data that was cleanly received in the absence of ionospheric scintillation. Next and second complete frame of raw IF GPS data was recorded several minutes later. Scintillation is simulated and added to the raw data before carrier recovery takes place. During tracking the data bits from the clean signal are imported, aligned with the current signal, and utilized as a training sequence whenever the bits overlap. Note from Figure 3.7 overlap only occurs during the TLM of each subframe and the data message of subframes 1-3; these are the only regions that the clean data can be used for training. When training data is not available, the receiver reverts back to the DPAT algorithm since previous work shows this discriminator has the best performance of those tested.

The experiments conducted assume accurate timing recovery and align the training sequence and current signal; the overlapping regions are specified in the carrier recovery scripts. This procedure is outlined using a block diagram in Figure 3.11.

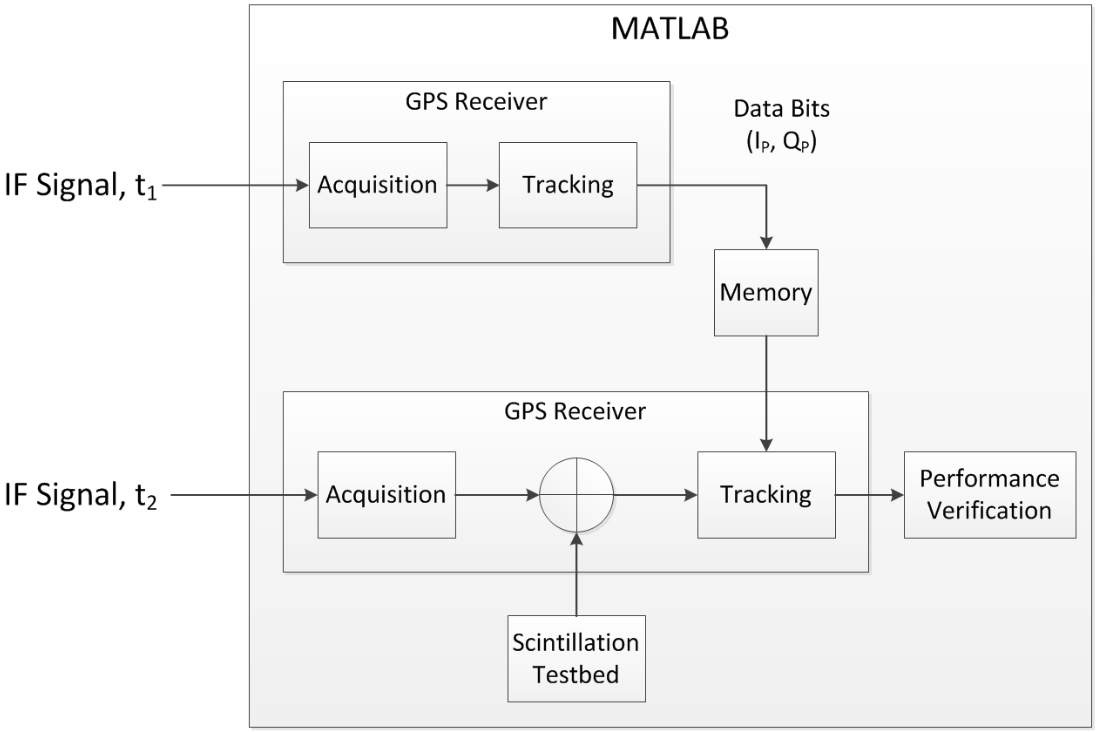

Figure 3.11: Block diagram outlining GPS processing with training data. The first IF signal is cleanly processed without adding any scintillation; the output data bits are saved to memory. A second IF signal is recorded; this one is actually used to determine the performance of the carrier recovery algorithms in use. The scintillation channel is added to this signal and data recorded previously is used as a training sequence to aid in carrier recovery.

Training Method 1 The first discriminator used is a training-based decision-directed algorithm based closely on the DD-AT discriminator presented in [14]. The DD-AT discriminator utilizes a 4-quadrant arctangent to detect phase errors up to pi radians and achieves data wipe-off by using the sign function to estimate the current bit. To implement training data, the sign of the current bit is replaced with the sign of the corresponding bit located in the training data. The phase error is computed as follows:

$$\phi_e = \mathrm{atan2}(Q_{P_k} \cdot \mathrm{sign}(I_{P_{k-1}}), I_{P_k} \cdot \mathrm{sign}(I_{P_{k-1}})) \tag{3.3}$$

where I_{P_k} and Q_{P_k} are the current (kth) in-phase and quadrature prompt correlator outputs, respectively, and $I_{P_{k-1}}$ is the in-phase prompt correlator output of the previous (k-*1*th) data bit.

A 3D mesh of the discriminator error magnitude is shown below in Figure 3.12. The figure on the left shows the error when a data bit '1' is transmitted and the figure on the right shows the error when a data bit '-1' is transmitted. The x- and y-axes represent all possible in-phase and quadrature prompt correlator outputs, respectively. The magnitude of the error is represented by the height of the z-axis (as well as the color map). Note that in both cases the error converges to zero when both the quadrature component is minimized and the in-phase component is equal to the transmitted data bit. So for example in the left figure when a data bit '1' is transmitted, even when the quadrature component is zero, the error is still maximum if the in-phase component is equal to -1.

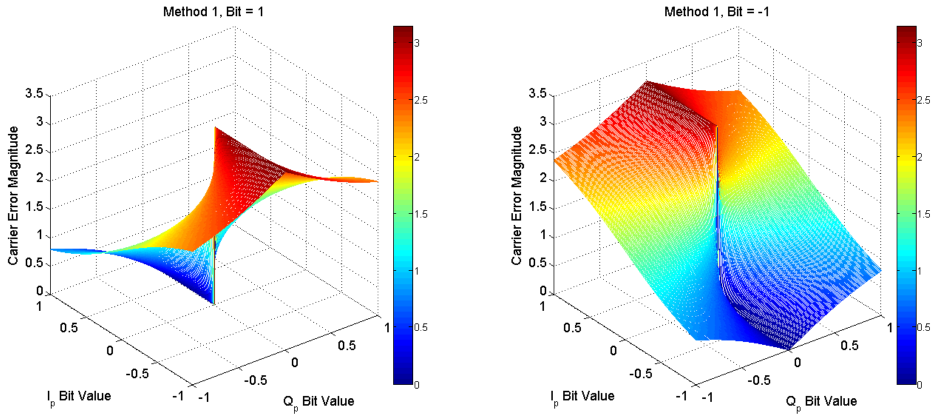

Figure 3.12: Surface mesh of the error magnitude for demodulated I and Q values. The left plot shows the error when a data bit '1' is transmitted; the right plot shows the error when a data bit '-1' is transmitted. The x- and y-axes represent the in-phase and quadrature values. The vertical axis shows the phase error magnitude returned by the discriminator. Note that the error is minimum when both the quadrature component is minimized and the in-phase value is the same as the transmitted data bit.

Training Method 2 The second training method is also a training-based decision-directed method but achieves data wipe-off using an arcsine function instead of the 4-quadrant arctangent. The arcsine can only detect up to $\pm\pi/2$ phase rotations. Although contradictory to the design specifications, this discriminator was selected to provide a comparison for a training-based Costas implementation. The discriminator algorithm, as described in [4], is modeled as follows:

$$\phi_e = \sin^{-1}\{\frac{\mathrm{imag}((I_{P_k} + jQ_{P_k}) \cdot (I_{P_{k-1}} - jQ_{Pk-1}))}{|I_{P_k} + jQ_{P_k}| \cdot |I_{P_{k-1}} + jQ_{Pk-1}|}\} \tag{3.4}$$

where I_{P_k} and Q_{P_k} are the current (kth) in-phase and quadrature prompt correlator outputs, respectively, and $I_{P_{k-1}}$ and $Q_{P_{k-1}}$ are the in-phase and quadrature, respectively, prompt correlator outputs of the previous (k-*1*th) data bit.

A 3D mesh of the discriminator error magnitude is shown below in Figure 3.13. Note that because this discriminator is insensitive to phase rotations greater than $\pm\pi/2$ the discriminator error is the same whether a data bit '1' or '-1' is transmitted. The x- and y-axes represent all possible in-phase and quadrature prompt correlator outputs, respectively. The magnitude of the error is represented by the height of the z-axis (as well as the color map). The error converges to zero when both the quadrature component is minimized and the in-phase component is maximized, though not necessarily the same value as the transmitted bit.

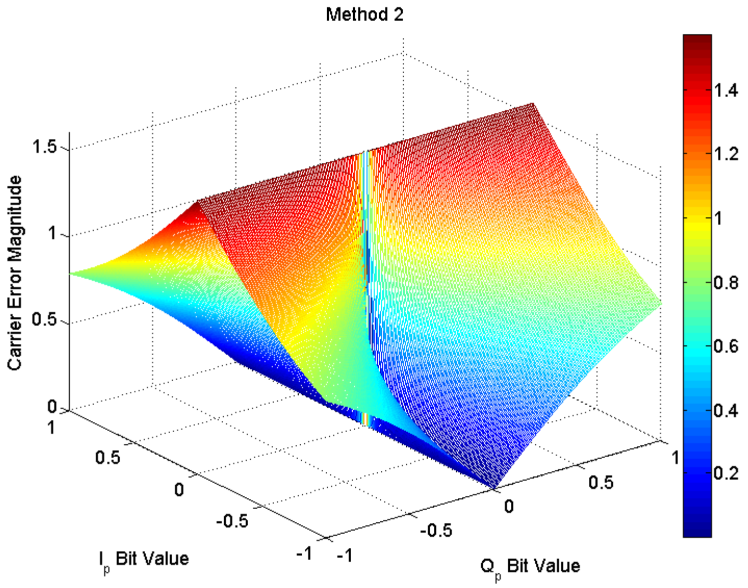

Figure 3.13: Surface mesh of the error magnitude for demodulated I and Q values. The discriminator error is the same regardless of the transmitted data bit. The x- and y-axes represent all possible in-phase and quadrature values. The vertical axis shows the phase error magnitude returned by the discriminator. The error is minimum when both the quadrature component is minimized and the in-phase value is maximized.

3.4 Testbed Assumptions

In order to simplify the problem of reducing loss of lock and improving carrier recovery performance, several assumptions must be made.

- This testbed assumes the GPS receiver has already achieved lock and is successfully tracking the GPS signal before scintillation occurs. Outside of simulation in practice, this assumption will likely hold considering that scintillation is abrupt, occurs spontaneously, and the most severe effects of scintillation generally last no longer than several seconds [15].
- The scintillation vector is generated using different S4 coefficients ranging from 0.2 to 1.2, but uses decorrelation time τ_0 fixed at 0.5 seconds. The S4 range was determined based on typical S4 ranges and τ_0 was selected to replicate severe scintillation conditions. These values are similar to those used in the testbed developed by Humphreys, et al [14].
- Subframes 1-3 were successfully recorded prior to scintillation and are still repeating when scintillation takes place. This assumption is necessary to test the performance of training-based carrier recovery techniques. In practice, this is a viable assumption because GPS satellite ephemeris data is generally valid for up to several hours [41].
- The purpose of this thesis is to characterize the performance of the carrier recovery methods during periods of scintillation. As such, this testbed does not actually compute a position fix or take into account positioning errors when measuring the performance of each carrier recovery scheme. The only metrics for measuring performance are the BER are mean time between cycle slips, both of which are determined using a cleanly demodulated signal with no scintillation added.
- Carrier tracking performance in this testbed is being evaluated for a single satellite signal (single PRN code). In an actual GPS receiver, several signals will be simultaneously decoded and at least four satellites would be necessary to obtain a position fix.

As mentioned previously, navigation processing is not being considered as a measure of performance so to simplify the experiments, only a single PRN code is evaluated throughout the entire experiment.

3.5 Chapter Summary

This chapter discusses the software and hardware components of the GPS scintillation testbed. Performance comparison of the USRP2 and USRP N210 shows the latter has improved RF properties and is thus the choice software radio frontend platform. Existing MATLAB GPS processing scripts and scintillation testbed are combined to create a method of adding a scintillation channel to complex baseband data during post-processing. An analysis of the GPS frame structure shows that subframes 1-3 repeat periodically and could potentially be used for training data. To test this hypothesis, a decision-directed PLL discriminator is modified to achieve data wipe-off using this training sequence.

Chapter 4

Experimentation and Results

The purpose of this chapter is to discuss the experimentation with each of the receiver models discussed in the previous chapter. The first section describes the methodology for testing the receiver performance. Initial results and an analysis will be provided, followed by modified design considerations which are used to devise second experiment. Finally the two results will be compared and used to determine the performance of training-based carrier recovery methods.

4.1 Methodology

Implementing each of the discriminator models into the PLL of the GPS receiver is fairly straightforward. The GPS processing scripts are all implemented in open-source Matlab code so the scripts containing the PLLs are modified accordingly. Scintillation is a random event so the performance of any of the discriminators cannot be accurately measured using a single iteration. To accurately characterize and compare the expected performance of each model, each discriminator is utilized numerous times and under varying scintillation intensities. The procedure for testing the performance is outlined as follows: First a scintillation vector with a specified S4 intensity and decorrelation time $\tau_0 = 0.5$

is generated. Next the same scintillation vector is used for all of the receiver models; the demodulated data bits and other information generated by the receiver (such as carrier frequency and PLL phase error) are saved after each iteration. After all discriminators have processed the same data file using the same scintillation vector, a new scintillation vector of the same intensity is generated; the process is completed 10 times. After 10 iterations, the process repeats but increases the S4 scintillation intensity by 0.1. In all, scintillation intensities varying from S4 = 0.2 to 1.2 are tested, each 10 times, for a total of 110 iterations per discriminator. The procedure is outlined in the following flow-graph:

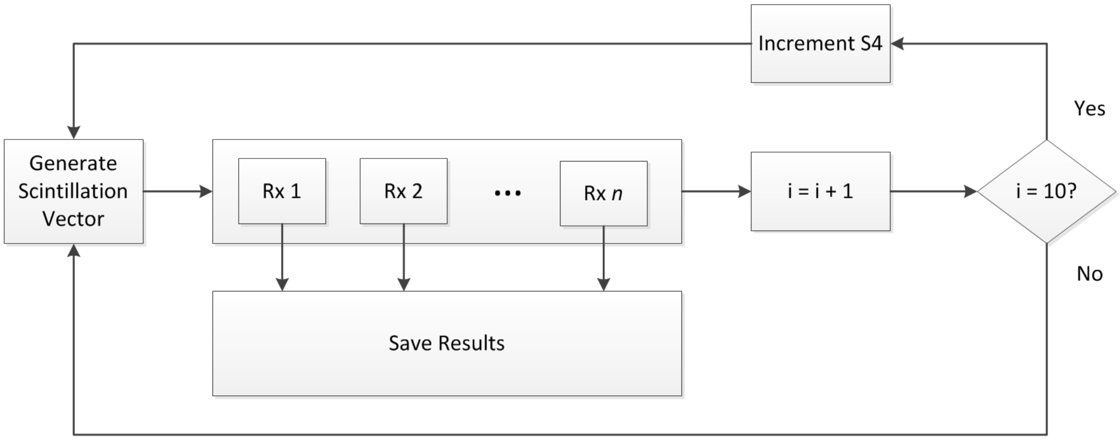

Figure 4.1: Block diagram outlining method of testing each receiver model. Mutliple scintillation vectors of varying intensity (S4 index) are generated. To fairly compare each model, the same scintillation vectors are used for all receivers.

The different carrier recovery schemes evaluated are summarized in Table 4.1. Refer to the previous chapter for additional information and explanation of the operation of each algorithm.

Table 4.1: Carrier Recovery Discriminators

Discriminator	Algorithm	Description
AT	$e = atan(Q_{P_k}/I_{P_k})$	Costas implementation returns phase error; this method is insensitive to π phase rotations.
DD-AT	$e = atan2(Q_{P_k}\text{sign}(I_{P_{k-1}}), I_{P_k}\text{sign}(I_{P_{k-1}}))$	Decision-directed 4-quadrant arctangent; wipe-off is achieved using the sign of the previous data bit.
DP-AT	$e = atan2(Q_{P_k}d_{P_k}, I_{P_k}d_{P_k})$	Decision-directed 4-quadrant arctangent; wipe-off is achieved by taking the dot product of the current correlator output $I_{P_k} + jQ_{P_k}$ with the phase change between bits (see 2.12b).
Training, v1	$e = atan2(Q_{P_k}\text{sign}(I_{P_t}), I_{P_k}\text{sign}(I_{P_t}))$	Training-based decision-directed method; I_{P_t} refers to the in-phase prompt correlator output from the training data.
Training, v2	$e = asin(\frac{\text{imag}(A_{P_k}A_{P_t}*)}{\lvert A_{P_k}\rvert \cdot \lvert A_{P_t}\rvert})$	Training-based decision-directed algorithm. A_{P_k} and A_{P_t} refer to the prompt correlator output of the current data and training data, respectively. This method is insensitive to π phase rotations and is used to provide a comparison to the AT Costas implementation.

4.2 Preliminary Experiment

The first set of experiments utilized five different discriminators: a traditional Costas implementation using a 2-quadrant arctangent, the two decision-directed methods described in [14], and the two training-based methods described in the previous chapter. Each discriminator was tested over varying scintillation intensities of S4 indices from 0.2 to 1.2. For S4 values less than 0.4, scintillation has almost no effect on the GPS signal. S4 values between 0.4 and 0.8 are characteristic of moderate scintillation and S4 values exceeding 0.8 indicate severe scintillation.

4.2.1 Performance Comparison

The performance of each of the carrier tracking schemes is determined by the bit error rate (BER) and the mean time between cycle slips (as this is the metric used in [14]). Figures 4.2 and 4.3 provide a comparison of the BER and mean time between cycle slips, respectively, for each of the implementations. The data for each metric is presented as a 3D histogram where each color represents a different scintillation intensity (denoted by S4 index) and each bar represents a different iteration conducted at each S4 value. Scintillation channels were generated 10 times at each intensity, producing a total of 110 data points per discriminator. The height of each bar (z-axis) in Figure 4.2 represents the BER of the specific iteration. Similarly, the height of each bar (z-axis) in Figure 4.3 denotes the time between cycle slips. Since the GPS signal used for testing each carrier tracking lasts only 30 seconds, a cycle slip period of 30 seconds denotes that no more than one cycle slip occurred during the entire sweep iteration.

For low scintillation intensities, the mean time between cycle slips is near 30

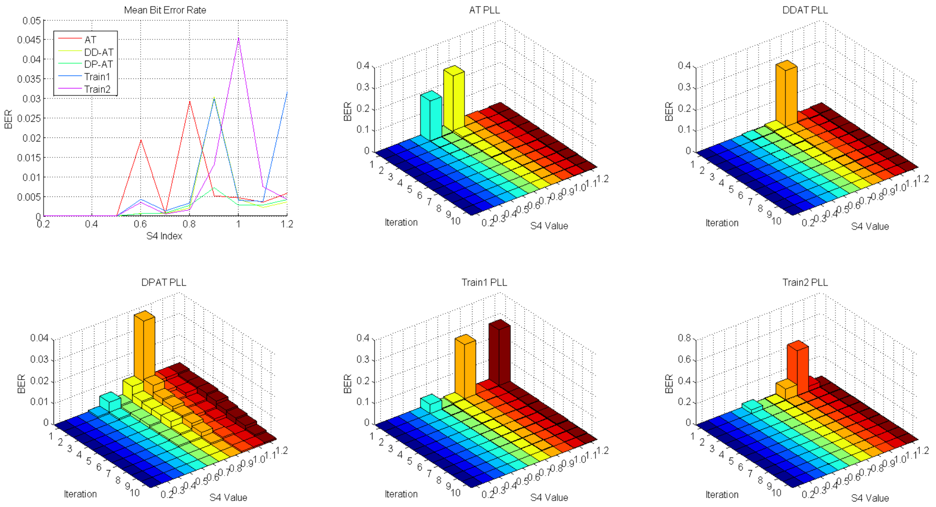

Figure 4.2: Bit Error Rate (BER) comparison across the different discriminators. The upper left plot shows the mean BER performance for all five implementations. Each 3D histogram subplot shows the BER for the individual discriminator algorithms. The color rows (x-axis) indicate a specific S4 value (scintillation intensity). The iteration (y-axis) refers to the trial number. The height of each bar (z-axis) corresponds to the BER of that specific iteration.

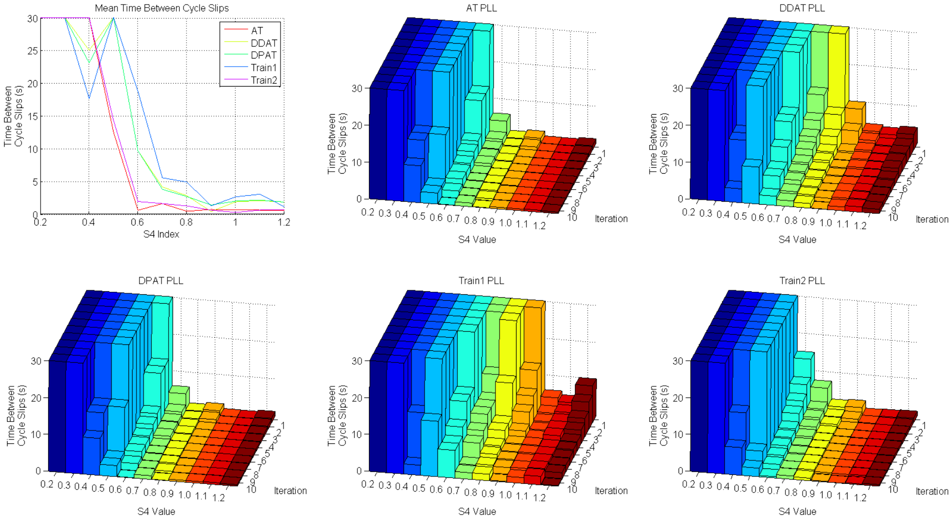

Figure 4.3: Comparison of the mean time between cycle slips for each of the five discriminators. The upper left figure shows the mean time between cycle slips for all five implementations. The color rows (x-axis) indicate a specific S4 value (scintillation intensity). The iteration (y-axis) refers to the trial number. The height of each bar (z-axis) corresponds to the time between cycle slips (in seconds). Since the signal length is only 30 seconds, a height of 30 indicates no more than one cycle slip occurred during processing.

Note that there are several instances when the BER is exceedingly high, notably larger than the mean values. Each of these outliers is indicative of frequency unlock and will be further discussed in the following section.

4.2.2 Observations

As shown in the figures above the training versions have slightly worse performance compared to the two decision-directed discriminators. The specific cases of interest are when the carrier recovery loop loses lock, either temporarily or completely. Certain discriminators lose lock while others are successful. Analyzing the successes and failures of each discriminator under particular conditions helps to better characterize the problem scintillation presents to carrier tracking. In turn, this information can be used to develop an even better, more robust tracking algorithm.

Case 1: Successful Tracking

The first scenario of interest is when the PLL successfully maintains lock on the signal. In this case the PLL does exactly what it is supposed to: track the signal. When frequency unlock does not occur, Training methods 1 and 2 show comparable to slightly-worse BER performance compared to the DDAT and DPAT implementations. Training method 1 also shows improvements in mean time between cycle slips. However, Figure 4.2 shows that none of these discriminators is immune to frequency unlock. The DPAT discriminator clearly yields the best performance, consistently maintaining a BER below 1 percent in all but one case. During one iteration of scintillation intensity S4 = 0.9, the BER approaches 0.4, denoting a short period of temporary frequency unlock. However this is still an order of magnitude less than the worst case BER of every other discriminator. This experiment accurately reflects the results collected by by Humphreys, et al in [14] in which the DPAT discriminator yielded the best tracking performance under strong scintillation conditions.

Case 2: Temporary Loss of Lock

The second case of interest is when the PLL temporarily loses lock but regains tracking before the end of the 30 second long signal. Understanding how the tracking loops are able to reestablish lock could provide insight to developing algorithms with short reacquisition times.

One critical factor that determines whether a PLL will be able to reacquire lock or not is the amount of time the PLL remains unlocked. For example in the case shown below in Figure 4.4, the tracked carrier frequency is only momentarily disrupted for only about 50 ms. Although the PLL phase error suffers several cycle slips during this period, this scenario suggests that the number of cycle slips experienced isn't as critical to tracking as the length of time in which the cycle slips take place.

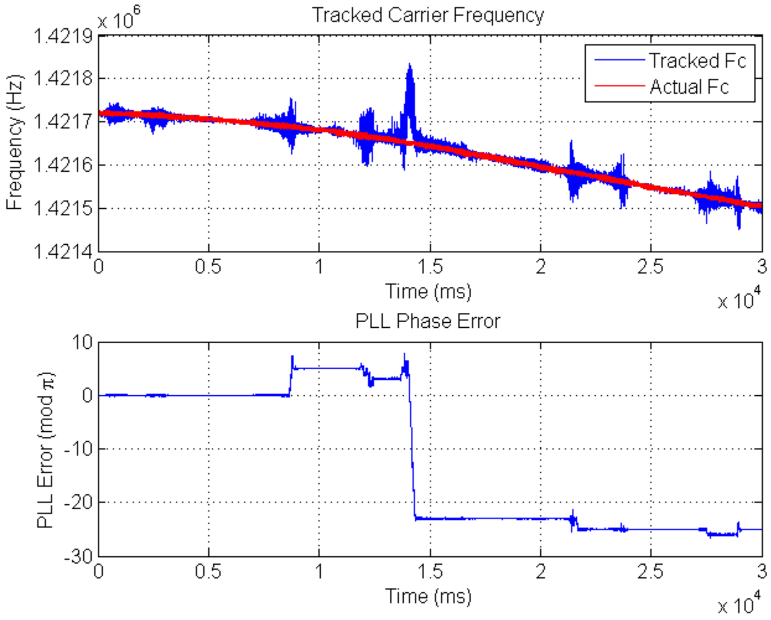

Figure 4.4: Relationship between carrier frequency and cycle slips for the 2-quadrant arctangent (AT) discriminator. The top figure shows the tracked carrier frequency in blue and the actual carrier frequency for reference in red. The bottom figure shows the PLL phase error, modulo pi. The spike in the estimated carrier frequency at time t=14 s corresponds to the rapid cycle slips that occur at the same time. Despite a PLL phase error of nearly 25 pi, the short duration enables the PLL to quickly reacquire the signal.

Another scenario shown in Figure 4.5 helps support this hypothesis. Similarly, a short period of cycle slipping results in temporarily losing lock, as shown in the offset tracked carrier frequency. The PLL loses lock but quickly reacquires the signal about 2.5 seconds later.

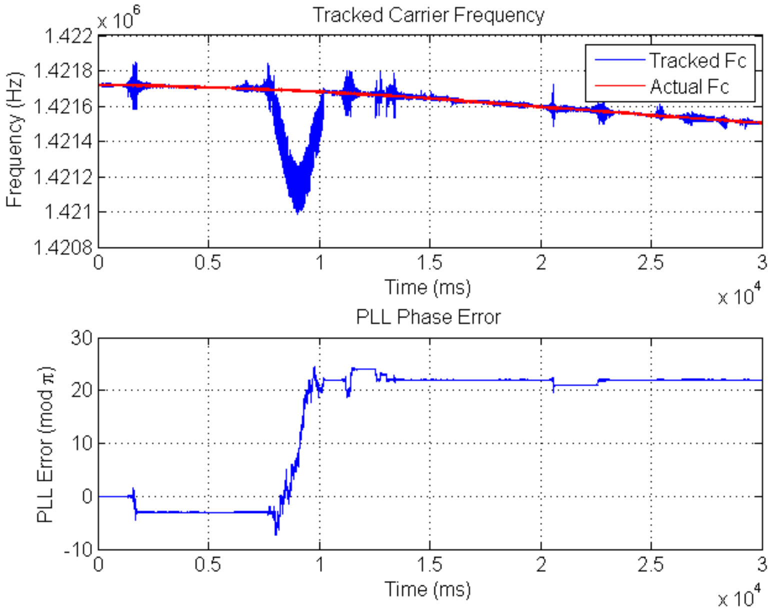

Figure 4.5: Relationship between carrier frequency and cycle slips for the 4-quadrant dot product (DPAT) discriminator. The top figure shows the tracked carrier frequency in blue and the actual carrier frequency for reference in red. The bottom figure shows the PLL phase error, modulo pi. The spike in the estimated carrier frequency at time t=8 s corresponds to the rapid cycle slips that occur at the same time. Despite a PLL phase error of about 22 pi, the short duration enables the PLL to quickly reacquire the signal.

Case 3: Total Loss of Lock

The third case that will be investigated is total loss of lock. Total loss of lock occurs when the PLL's estimate of the carrier frequency drifts further away from the actual value to the point where it is no longer able to recover.

Two interesting cases are shown below. In the first, shown in Figure 4.6, the PLL phase error is much less than that experienced in either of the previous two methods yet the cycle slips last for several seconds, possibly because the algorithm is slow to adapt to the phase changes. Based on this example, one possible method of improving carrier tracking performance would be to increase the convergence rate, or step size of the PLL.

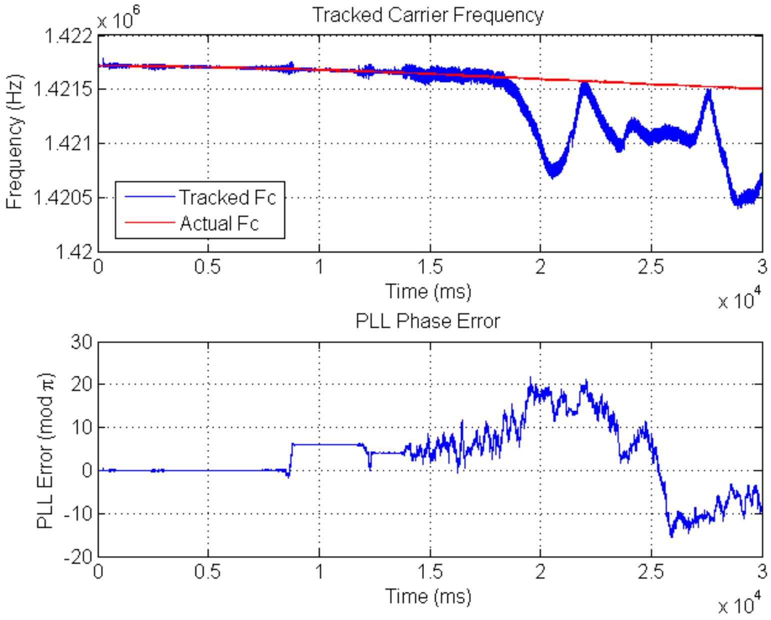

Figure 4.6: Relationship between carrier frequency and cycle slips for Training version 2. The top figure shows the tracked carrier frequency in blue and the actual carrier frequency for reference in red. The bottom figure shows the PLL phase error, modulo pi. The PLL begins to lose lock at about time t=14s.

A second scenario utilizing Training method 1, shown in Figure 4.7, reinforces the notion that the PLL must be quick to adapt to changes. In this case, the cycle slips last for over 3 seconds. However unlike the previous example, something interesting happens: the PLL reaches a steady state with near constant phase error but the carrier frequency remains uncorrected. The PLL has achieved a false lock; in other words, the PLL discriminator indicates the receiver is correctly tracking the signal when it is not. One possible explanation for this, as suggested in [21], is that the discriminator is minimizing the quadrature component but not maximizing the in-phase component. Training method 1's discriminator uses a 4-quadrant arctangent with error modeled in equation 3.3. Figure 3.12 shows this discriminator returns a minimum error when both the quadrature component is minimized *and* the in-phase component is maximized; therefore this is likely not the problem.

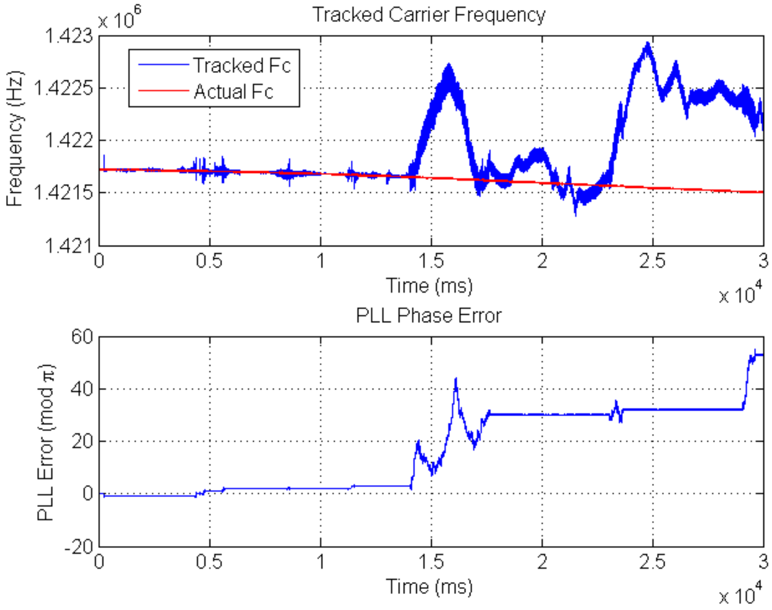

Figure 4.7: Relationship between carrier frequency and cycle slips for Training version 1.

A more plausible explanation suggested in [44] is false acquisition. After scintillation causes the PLL to lose lock of the carrier frequency the receiver must reacquire the signal in order to maintain tracking. Acquisition is achieved by correlating the known C/A code with the demodulated signal; the receiver will detect a high autocorrelation value when the signal is correctly demodulated by its actual carrier frequency. However false detection can occur when the receiver detects the autocorrelation of the C/A code with a sidelobe of the baseband signal. False acquisition most often occurs when the receiver utilizes a short integration time and received signal has a low C/N0 [21]. This receiver uses a short integration time of 1 ms (20 ms is considered a long integration time) and scintillation has severely degraded the C/N0.

A common solution to countering the problem of false detection is to increase the integration interval [21], [44]; however longer integration intervals increase the acquisition time. The integration time does not have to be constant and can be shortened or increased depending on the C/N0. The integration time for the initial acquisition cannot be based on C/N0 because C/N0 can only be computed once data bits have been demodulated. In the case of reacquisition however, C/N0 is available because data bits have already been received. Therefore a possible method to improving the receiver models and preventing loss of lock is to utilize an integration interval that varies depending on the value of the current C/N0.

4.2.3 Conclusions

Based on these observations, a robust carrier tracking scheme requires a PLL that can quickly adapt to a changing channel. To prevent loss of lock, the PLL must utilize a variable step size that increases as the carrier frequency drifts further from the actual value. The actual carrier frequency is unknown, however frequency drift has been shown to be highly correlated to the PLL phase error, cycle slips, and low C/N0. Therefore a tracking scheme is proposed that implements a variable integration time that increases as the C/N0 decreases.

4.3 Secondary Experiment

The second implementation tested builds upon the previous experiment utilizing the same discriminators. The difference in implementation is that the PLL error of each technique is computed using a variable integration time defined by:

$$\frac{C/N_{0_{nom}}}{C/N_0} * 10^{-3}\text{s} \tag{4.1}$$

where I is the integration time in seconds, C/N_0 is the current (instantaneous) C/N0 value, and $C/N_{0_{nom}}$ is the nominal C/N0 value; in this experiment, the nominal value is 43 dB-Hz.

The integration time is inversely proportional to the C/N0 so that the PLL will converge faster as the carrier frequency estimate drifts further from the actual value.

4.3.1 Peformance Comparison

Figure 4.8 provides a comparison of the bit error rates (BER) for each of the receiver models utilizing a variable integration time. The performance of this model is significantly worse than the version with the fixed integration time. Compared to the initial experiment this system loses frequency lock with a much higher frequency. The reader can see that there are several instances when the BER approaches the worst case value of 0.5.

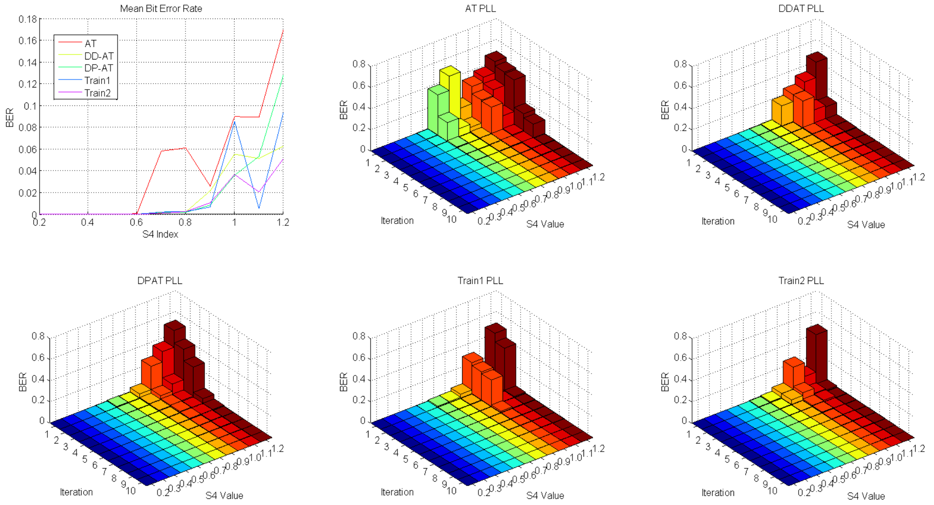

Figure 4.8: Bit error rate of each discriminator utilizing a variable integration time. The upper left plot shows the mean BER performance for all five implementations. Each 3D histogram subplot shows the BER for the individual discriminator algorithms. The color rows (x-axis) indicate a specific S4 value (scintillation intensity). The iteration (y-axis) refers to the trial number. The height of each bar (z-axis) corresponds to the BER of that specific iteration.

4.3.2 Observations

Investigation into the loss of lock cases reveals a severe flaw in the implementation of the variable integration time. As the instantaneous C/N0 value approaches zero, the integration time approaches infinity, as shown in Figure 4.9. This flaw was overlooked because the minimum C/N0 occurring during scintillation periods was underestimated. However one possible solution to this problem could be to cap the integration time with a lower bound, regardless of the amplitude of the instantaneous C/N0.

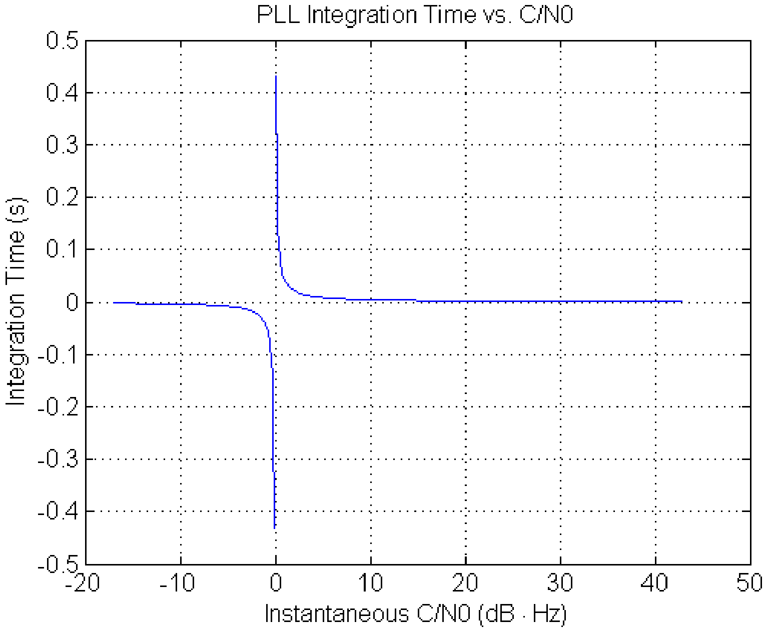

Figure 4.9: Variable integration time computed as a function of instantaneous C/N0. As the C/N0 value approaches zero, the integration time approaches infinity.

However these results can still prove useful in determining the maximum integration time one should use with low probability of loss of lock. All cases when the tracking loops lost lock in excess of 5 seconds (cumulative over the 30 second signal range) were analyzed to determine specifically what caused loss of lock. As the integration time increases to several milliseconds, the carrier frequency estimate will rapidly shift away from the actual value, as shown in Figure 4.10. The sharp transitions are a result of long integration times generated as the instantaneous C/N0 approaches zero.

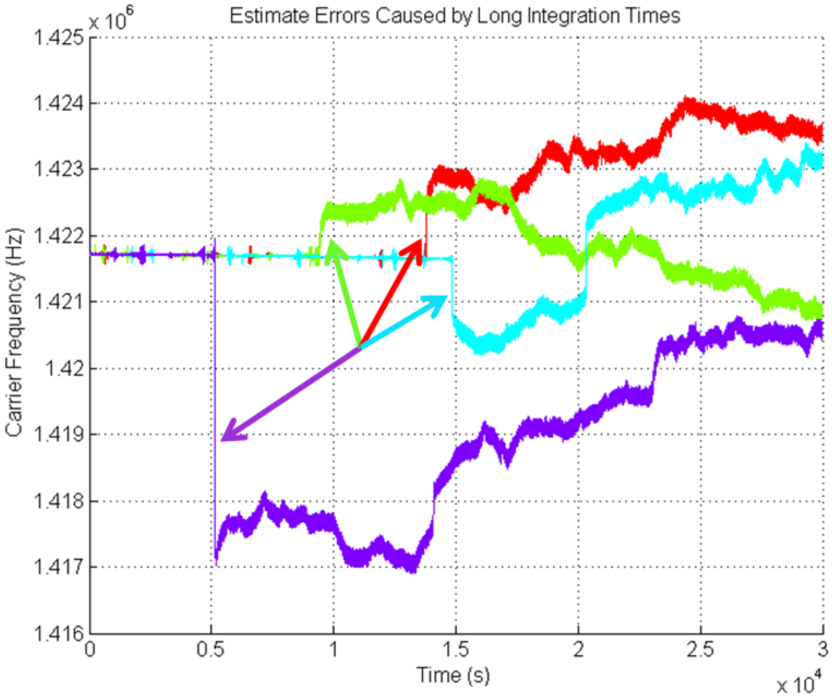

Figure 4.10: Plot of the estimated carrier frequency for Training method 1 iterations suffering loss of lock. Arrows denote where frequency unlock occurs. The near-instantaneous change in frequency is indicative that the integration time is too long and thus causing the rapid fluctuations.

Of 36 cases when the PLL lost lock for at least 5 seconds, 28 iterations (77.8 percent) show rapid carrier frequency offsets similar to those shown above. This suggests a long integration period is the cause of frequency unlock in these samples. Determining the integration time when unlock occurred could help provide a useful estimate for the largest integration time that should be used in order to have a low probability of frequency unlock while improving tracking performance. Figure 4.11 shows how often frequency unlock occurred at a given C/N0 value within these 28 samples. The mean C/N0 value is 10.865 dB-Hz with a standard deviation of 5.765. This means that if frequency unlock is caused by an excessively large integration time, frequency lock will be maintained approximately 95 percent of the time if the C/N0 remains above 22.39 dB-Hz. Referring back to the model for the integration time in 4.1, this C/N0 value corresponds to a period of about 2 ms.

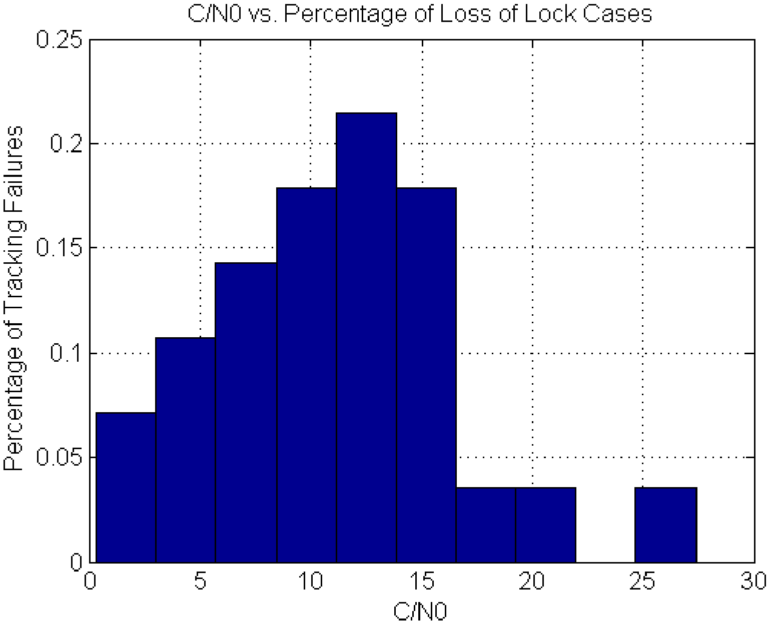

Figure 4.11: Histogram showing the percentage of tracking failure cases that result in loss of lock at a specific instantaneous C/N0 value. The y-axis reflects the percentage of the 28 cases when frequency unlock lasted at least 5 seconds at the indicated C/N0. The mean C/N0 value is 10.865 dB-Hz with a standard deviation of 5.765.

4.3.3 Conclusions

Carrier tracking can be improved, especially during periods of low C/N0, by increasing the integration time of the phase locked loop. However using a step size that is too large can cause the estimate of the carrier frequency to quickly drift far away from the actual value. The integration period must be selected carefully depending on the signal and channel properties. The results from this simulation are used to determine a rough estimate for the maximum integration time that should be selected to reduce the frequency of cycle slips resulting from a large step size. The following section describes the results acquired using a slightly modified design based on the findings of this experiment. Further research and methods for optimizing the step size under scintillation conditions is left for future work.

4.4 Tertiary Experiment

Based on the average performance established in the previous section, a revised model for the integration time is represented by:

$$I = \begin{cases} .001\text{s} & C/N_0 > C/N_{0_{nom}} - 10\text{dB}\cdot\text{Hz} \\ \frac{C/N_{0_{nom}}}{C/N_0} * 10^{-3}\text{s} & C/N_{0_{nom}} - 23\text{dB}\cdot\text{Hz} < C/N0 \leq C/N_{0_{nom}} - 10\text{dB}\cdot\text{Hz} \\ .002\text{s} & C/N_0 \leq C/N_{0_{nom}} - 23\text{dB}\cdot\text{Hz} \end{cases} \tag{4.2}$$

where I is the integration time in seconds, C/N_0 is the current (instantaneous) C/N0 value, and $C/N_{0_{nom}}$ is the nominal C/N0 value; in this experiment, the nominal value is 43 dB-Hz. An integration time of .002 seconds was selected as the default period for deep fades exceeding 23 dB from the nominal C/N0 value. In the previous section, this integration time was determined to be a good estimate for a longer integration time that reduces the probability of frequency unlock.

4.4.1 Performance Comparison

The bit error rate (BER) of each discriminator is shown below in Figure 4.12. The upper left plot shows the mean BER performance for all 5 implementations. Each 3D histogram subplot shows the BER for the individual discriminator algorithms. The color rows (x-axis) indicate a specific S4 value (scintillation intensity). The iteration (y-axis) refers to the trial number. The height of each bar (z-axis) corresponds to the BER of that specific iteration.

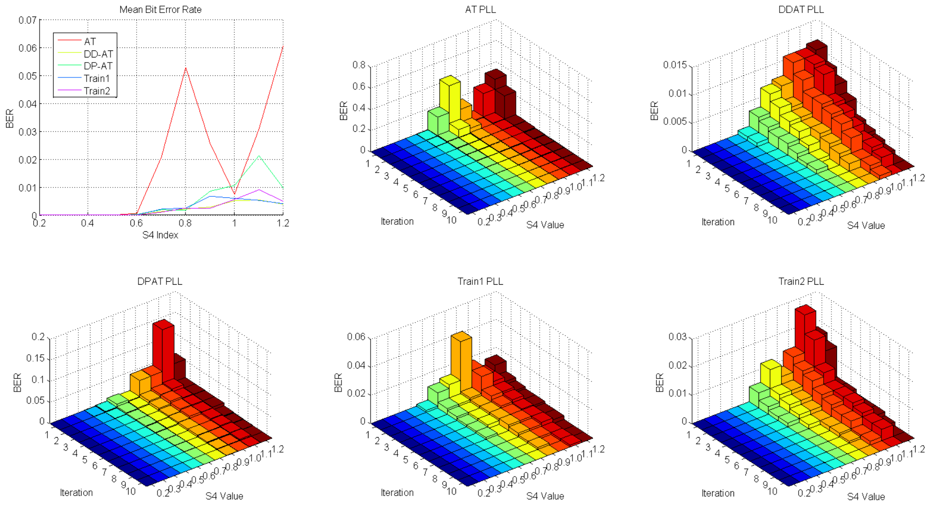

Figure 4.12: Bit Error Rate (BER) comparison across the different discriminators. The upper left plot shows the mean BER performance for all 5 implementations. Each 3D histogram subplot shows the BER for the individual discriminator algorithms. The color rows (x-axis) indicate a specific S4 value (scintillation intensity). The iteration (y-axis) refers to the trial number. The height of each bar (z-axis) corresponds to the BER of that specific iteration.

4.4.2 Observations

Aside from the 2-quadrant arctangent discriminator, all of the other implementations show significant improvements in tracking stability and ability to maintain lock. The DDAT and Training method 1 implementations yield the best performance with a mean BER below 0.6 percent and 0.7 percent, respectively, even with high intensity scintillation.

Figure 4.13 shows the tracked carrier frequency and PLL phase error of the received signal using a fixed integration time and a variable integration time. For comparison, the actual carrier frequency is also provided. Although the receiver utilizing a variable integration time still suffers cycle slips, the PLL is able to quickly recover and maintain lock for the duration of the signal.

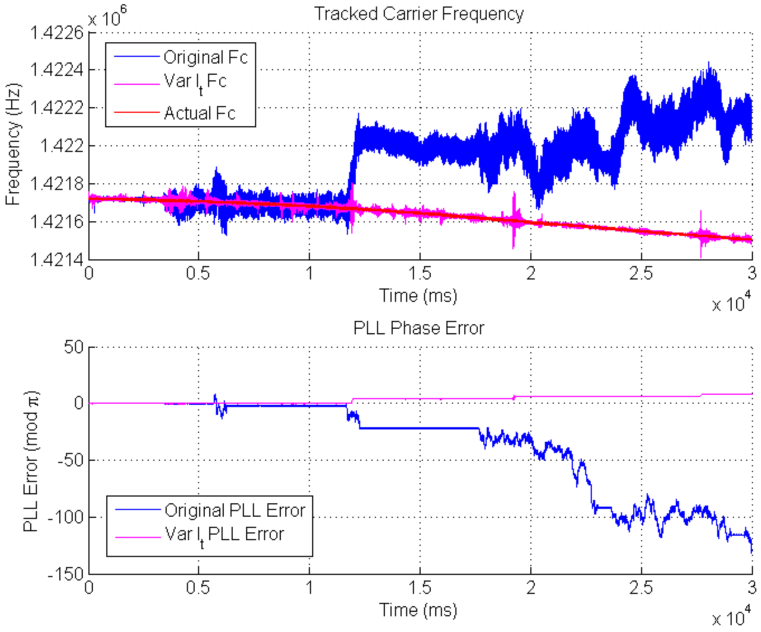

Figure 4.13: The top plot shows the estimated carrier frequency using a fixed integration time (blue) and variable integration time (magenta). For comparison, the actual carrier frequency is provided in red. The bottom plot shows the PLL phase error using a fixed integration time (blue) and variable integration time (magenta).

The results of this experiment are summarized in the following two tables. Table 4.2 shows the bit error rate for each discriminator at 4 different scintillation intensities. Table 4.3 shows the mean time between cycle slips for each discriminator at the same scintillation intensitites. For comparison, the mean time between cycle slips obtained by Humphreys, et al in [14] is presented in Table 4.4.

Table 4.2: BER Using Variable Integration Time

Discriminator	S4=0.6	S4=0.8	S4=1.0	S4=1.2
AT	1.336E-4	5.270E-02	7.40E-3	6.053E-02
DD-AT	1.336E-4	2.200E-03	5.133E-3	3.933E-03
DP-AT	2.667E-4	1.800E-03	10.60E-3	9.600E-03
Train, v1	1.333E-4	2.533E-03	6.00E-3	4.067E-03
Train, v2	0	2.533E-03	5.60E-3	4.933E-03

Table 4.3: Mean Time Between Cycle Slips Using Variable Integration Time

Discriminator	S4=0.6	S4=0.8	S4=1.0	S4=1.2
AT	6.383 s	0.2443 s	0.5814 s	0.2026 s
DD-AT	17.65 s	3.529 s	1.863 s	1.961 s
DP-AT	16.67 s	3.333 s	0.8696 s	1.128 s
Train, v1	9.375 s	2.679 s	1.261 s	1.333 s
Train, v2	4.615 s	1.345 s	0.6186 s	0.7229 s

Table 4.4: Mean Time Between Cycle Slips, Empirical Results from Humphreys, et al [14]

Discriminator	S4 0.6
AT	33.6 s
DD-AT	37.0 s
DP-AT	43.3 s

Although the values are off by nearly an order of magnitude, the trends between the two results are fairly consistent in that the DPAT discriminator yields better performance than the AT. One possibility for the discrepancy is that Humphreys, et al simulated scintillation using lower scintillation intensity. It is also possible their PLLs were using different noise bandwidths and integration times, both of which have a profound effect on the PLL's tracking ability.

4.4.3 Conclusions

This experiment shows that the decision directed 4-quadrant arctangent when coupled with a variable integration time yields the best overall performance over a wide range of scintillation intensities. Compared to the first experiment which used a fixed step size, carrier tracking can be greatly improved using a variable integration time with step size that increases as C/N0 decreases. However a step size too large can result in rapid frequency unlock. Research to determine optimal carrier step sizes will be left for future work.

4.5 Summary

A comparison of the mean BER and mean time between cycle slips for each of the three experimental trials is shown in Figures 4.14 and 4.15, respectively.

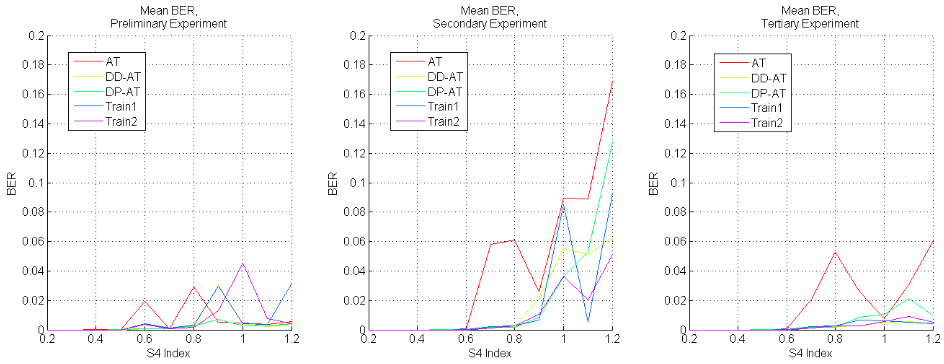

Figure 4.14: Mean BER (from left to right) of preliminary, secondary, and tertiary experimental implementations.

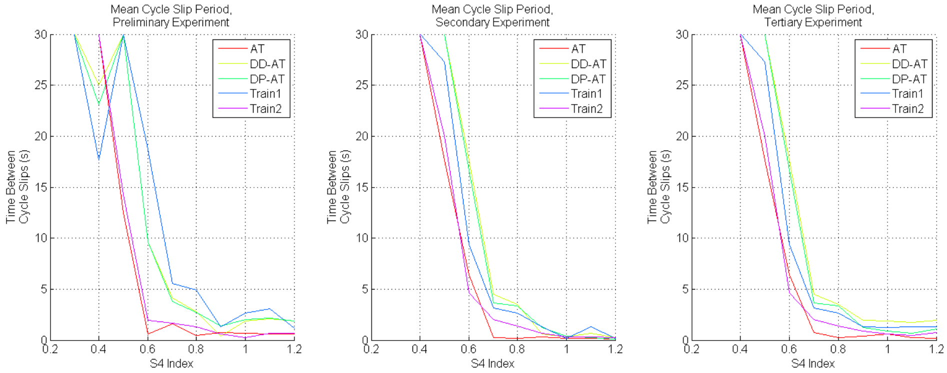

Figure 4.15: Mean time between cycle slips (from left to right) of preliminary, secondary, and tertiary experimental implementations.

These experiments show that training-based decision-directed PLLs do not noticeably improve carrier tracking performance. Aside from carrier tracking, the training sequence may be better utilized in some other component of the receiver. For example, training data may be well suited for an equalizer or it could be used to compute bit error rates that could control the integration time. On a similar note, training-based algorithms utilizing variable integration times show improved tracking performance during scintillation conditions compared to fixed integration times. Loss of lock can be prevented by increasing the step size as C/N0 decreases. Although larger step sizes accelerate loop convergence, integration periods that are too large can cause rapid carrier frequency fluctuations which lead to temporary or even total loss of lock. There is an intricate relationship between the C/N0 and optimal step size that should be selected to minimize the probability of frequency unlock.

The training methods that were tested both require longer reacquisition times (compared to existing algorithms) when frequency unlock occurs. When the signal suffers rapid and sequential deep fades the training methods are not as well suited for reacquisition. When coupled with a variable integration time, the decision-directed 4-quadrant arctangent (DDAT) discriminator yields the best performance in terms of BER and mean time between cycle slips. This discriminator yields better performance than the training versions because it is better suited to quickly adapt to the rapid phase and amplitude fluctuations caused by scintillation.

Chapter 5

Conclusions

This chapter summarizes the achievements of this thesis and relevant topics to be further studied in future work. Achievements includes a description of the software GPS testbed, carrier recovery techniques developed, and experimental results. Future work discusses improvements that can be made to the testbed as well as alternative methods that should be investigated.

5.1 Research Achievements

Using existing MATLAB GPS processing scripts and scintillation models, a testbed for adding a scintillation channel during post-processing was developed. This testbed was used to replicate scintillation conditions on complex baseband data recorded using the USRP software radio platform. Experimental results show the testbed accurately replicates scintillation conditions.

Research into the GPS frame structure shows that ephemeris data could prove useful as a training sequence because it repeats periodically. Assuming a clean transmission is received prior to scintillation occurs, this data could be used to improve the carrier tracking performance and reduce loss of lock. To test this hypothesis, a decision-directed

PLL discriminator algorithm was devised to use training data. Using BER and mean time between cycle slips as metrics, the performance of this new method and the current state of the art were compared.

Preliminary results showed the training-based algorithm fared worse, possibly because it was slow to accurately estimate the phase error. The slow convergence time suggested that utilizing a variable step size could improve the robustness of the tracking scheme. Experimental results using a variable integration time that increases as C/N0 decreases show that probability of loss of lock is decreased. These results show that the PLL's step size plays an integral role in the receiver's ability to maintain lock on a GPS signal.

5.2 Future Work

Decision-directed PLL methods have been shown, both in previous research and in this thesis, to outperform Costas loops during periods of ionospheric scintillation. Although the training-based carrier recovery schemes generally performed worse than discriminators utilizing differential bit detection, previously recorded GPS frames could potentially be used as training data under normal operating conditions. Even in the absence of scintillation, GPS signals are subject to a slew of other channel effects that can cause the receiver to return an incorrect position fix. Incorporating the training sequence for general operation could help to improve overall position accuracy and reduce pseudorange errors.

Another possibility is to utilize the training data in another component of the receiver. Training data can prove invaluable in any communications system, even if carrier recovery isn't the most appropriate function. Other potential applications include a GPS equalizer or use in the acquisition stage to reduce the initial time to lock. Or in the event that loss of lock occurs, training data could also be used to reduce the reacquisition period.

Experimentation with variable integration times shows that the PLL's step size plays a critical role in the ability to maintain lock during periods of scintillation. This thesis only investigates one method of relating step size to carrier to noise density ratio. However further research should be conducted to determine an optimal step size or method of determining an appropriate step size depending on signal properties including signal to noise ratio (SNR), bit error rate (BER), or instantaneous scintillation intensity (S4 coefficient).

Bibliography

[1] Sanjay Acharya, *Itu paves way for next-generation 4g mobile technologies*, Press Release, 2010.

[2] Catherine Alexandrow, *The story of gps*, [Online]: `http://www.darpa.mil/WorkArea/DownloadAsset.aspx?id=2565`, 2008.

[3] Gerd Ascheid and Heinrich Meyr, *Cycle slips in phase-locked loops: A tutorial survey*, IEEE Transactions on Communications **30** (1982), no. 10, 2228 – 2241.

[4] John R. Barry, Edward A. Lee, and David G. Messerschmitt, *Digital communication, third edition*, Springer, New York, New York, 2004.

[5] Dieter Bilitza, *International reference ionosphere 2000*, Radio Science **36** (2001), no. 2, 261 – 275.

[6] Kai Borre, Dennis M. Akos, Nicolaj Bertelsen, Peter Rinder, and Soren Holdt Jensen, *A software-defined gps and galileo receiver*, Birkhauser, 2007.

[7] Kelvin Case, [Online]: http://upload.wikimedia.org/wikipedia/en/e/e6/1000px-Atmosphere_layers-en.PNG, 2012.

[8] S. Datta-Barua, P.H. Doherty, S.H. Delay, T. Dehel, and J.A. Klobuchar, *Ionospheric scintillation effects on single and dual frequency gps positioning*, Proceedings of the

16th International Technical Meeting of the Satellite Division of The Institute of Navigation (ION GPS/GNSS 2003), 2003, pp. 336 – 346.

[9] Frank Van Diggelen, *A-gps: Assisted gps, gnss, and sbas*, Artech House, 2009.

[10] Kathleen Dunleavy, *Sprint 4g expansion plans to stretch coast-to-coast from los angeles to miami*, Press Release, 2010.

[11] Biagio Forte and Sandro M. Radicella, *Comparison of ionospheric scintillation models with experimental data for satellite navigation applications*, Annals of Geophysics **48** (2005), no. 3, 505 – 514.

[12] Bruce M. Hannah, *Modeling and simulation of gps multipath propagation*, Ph.D. thesis, Queensland University of Technology, 2001.

[13] Todd E. Humphreys, Mark L. Psiaki, Joanna C. Hinks, Brady O'Hanlon, and Paul M. Kintner Jr., *Simulating ionosphere-induced scintillation for testing gps receiver phase tracking loops*, IEEE Journal of Selected Topics in Signal Processing **3** (2009), no. 4, 707 – 715.

[14] Todd E. Humphreys, Mark L. Psiaki, and Paul M. Kintner Jr., *Modeling the effects of ionospheric scintillation on gps carrier phase tracking*, IEEE Transactions on Aerospace and Electronic Systems **46** (2010), no. 4, 1624–1637.

[15] Todd E. Humphreys, Mark L. Psiaki, Brent M. Ledvina, Alessandro P. Cerruti, and Paul M. Kintner Jr., *Data-driven testbed for evaluating gps carrier tracking loops in ionospheric scintillation*, IEEE Transactions on Aerospace and Electronic Systems **46** (2010), no. 4, 1609–1623.

[16] Information and Communication Technology (ICT) Statistics, *The world in 2011 ict facts and figures*, Tech. report, International Telecommunication Union, 2011.

[17] Randy James, *Gps*, [Online]: `http://www.time.com/time/magazine/article/0,9171,1901500,00.html`, 2009.

[18] Laila Jeong, *Communications/navigation outage forecasting system (c/nofs*, Tech. report, Air Force Research Laboratory Space Vehicles Directorate, 29 Randolph Rd., Hanscom AFB, MA 01731, 2010.

[19] C. Richard Johnson Jr., William A. Sethares, and Andrew G. Klein, *Software receiver design*, Cambridge University Press, Cambridge, United Kingdom, 2011.

[20] Angelo Joseph, *Gnss solutions: Measuring gnss signal strength*, InsideGNSS (2010), 20–25.

[21] Elliott Kaplan and Christopher Hegarty, *Understanding gps: Principles and applications, second edition*, Artech House, 2005.

[22] Paul M. Kinter Jr., M. Psiaki, T. Humphreys, A. Cerruti, B. Ledvina, A. Mannucci, D. Gary, E. de Paula, and L. Shelton, *A beginners guide to space weather and gps*, [Online]: `http://gps.ece.cornell.edu/SpaceWeatherIntro_update_2-20-08_ed.pdf`, 2008.

[23] Paul M. Kintner, Todd Humphreys, and Joanna Hinks, *Gnss and ionospheric scintillation: How to survive the next solar maximum*, InsideGNSS (2009), 22–30.

[24] Dennis L. Knepp, *Radar measurement of ionospheric scintillation in the polar region*, General Assembly and Scientific Symposium, 2011 XXXth URSI, 2011, pp. 1–4.

[25] S. Kumar and C. Zahn, *Mobile communications: Evolution and impact on business operations*, Technovation **23** (2003), no. 6, 515 – 520.

[26] Northwood Labs LLC, *Gps carrier-to-noise density*, AN101, feb 2003.

[27] Robert .J. Mackin Jr. and Marcia Neugebauer, *Jet Propulsion Laboratory Conference on the Solar Wind*, The Solar Wind, 1964.

[28] NASA, [Online]: `http://commons.wikimedia.org/wiki/File:GPS_Satellite_NASA_art-iif.jpg`, 2006.

[29] Navigation National Coordination Office for Space-Based Positioning and Timing, *The global positioning system*, [Online]: `http://www.gps.gov/systems/gps/`, 2013.

[30] Navstar, *Global positioning system directorate systems engineering and integration interface specification is-gps-200*, IS-GPS-200F, sep 2011.

[31] Kaveh Pahlavan and Prashant Krishnamurthy, *Principles of wireless networks*, Prentice Hall, 2002.

[32] Bradford W. Parkinson, Thomas Stansell, Ronald Beard, and Konstantine Gromov, *A history of satellite navigations*, Navigation **32** (1995).

[33] Joseph Petovello, *Gnss solutions: Satellite almanac life expectancy*, InsideGNSS (2008), 14–19.

[34] Ionospheric Prediction Service (IPS) Radio and Space Services, *Facts on space weather effects*, [Online]: `http://www.ips.gov.au/Category/Educational/Space%20Weather/Space%20Weather%20Effects/Facts_on_Space_Weather_Effects.pdf`.

[35] J.A. Secan, R.M. Bussey, and E.J. Fremouw, *High-latitude upgrade to the wideband ionospheric scintillation model*, Radio Science **32** (1997), no. 4, 1567 – 1574.

[36] James A. Secan, *The wbmod ionospheric scintillation model*, [Online]: http://www.nwra.com/ionoscint/wbmod.html, NorthWest Research Associates.

[37] Jiwon Seo, Todd Walter, Tsung-Yu Chiou, and Per Enge, *Characteristics of deep gps signal fading due to ionospheric scintillation for aviation receiver design*, Radio Science **44** (2009), no. 1.

[38] S. Skone, G. Lachapelle, D. Yao, W. Yu, and R. Watson, *Investigating the impact of ionospheric scintillation using a gps software receiver*, ION GNSS 2005 Conference, 2005.

[39] NASA/Goddard Space Flight Center Scientific Visualization Studio, [Online]: `http://svs.gsfc.nasa.gov/goto?3310`, 2005.

[40] Simon R. Suanders and Alejandro Aragón-Zavala, *Antennas and propagation for wireless communication systems*, second ed., Wiley, 2007.

[41] National Geodedit Survey, *Gps orbits*, [Online]: `http://www.ngs.noaa.gov/orbits/orbit_data.shtml`, 2013.

[42] Taoglas, *Which internal gps active patch antenna?*, Version 1, 2008.

[43] R. Tiwari, S. Skone, S. Tiwari, and S.J. Strangeways, *Wbmod assisted pll gps software receiver for mitigating scintillation affect in high latitude region*, General Assembly and Scientific Symposium, 2011 XXXth URSI, 2011, pp. 1 – 4.

[44] Phillip W. Ward, *Gps receiver search techniques*, Position Location and Navigation Symposium, 1996., IEEE 1996, 1996, pp. 604 – 611.

[45] W. Wongtrairat and P. Supnithi, *Average probability of bit error of mpsk in combined flat ionospheric scintillation and flat fading channels*, TENCON 2006. 2006 IEEE Region 10 Conference, nov, pp. 1–4.

[46] Helen E. Worth and Mame Warren, *Transit to tomorrow*, Whitney, 2009.